Numerical Analysis Of Bird Strike Damage On Composite Sandwich Structure Using Abaqus/Explicit

A project presented to the Faculty of Aerospace Engineering
San Jose State University
in partial fulfillment of the requirements for the degree
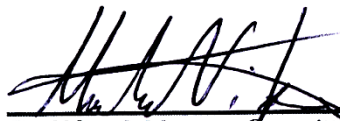Master of Science in Aerospace Engineering

by

Rahulkumar K. Mav

December 2013

San José State
UNIVERSITY

Approved by

Dr. Nikos J. Mourtos, Committee Chair   16 Dec 13
                                                                   Date

Prof. Gonzalo Mendoza, Committee Member   12/15/13
                                                                   Date

Dr. Cecilia Larrosa, Committee Member   12/15/2013
                                                                   Date

2

Table of Contents

List of Figures

List of Tables

Numerical analysis of Bird Strike Damage on Composite sandwich structure

Rahulkumar K. Mav
San Jose State University, San Jose, CA 95192

The present work shows extensive use of the non-linear dynamic finite element code to simulate a bird impact event on the composite sandwich wing leading edge rather than expensive full-scale gas-gun type of experimental method. Two sandwich panels used in these analyses consist of Aerospace Commercial Grade (ACG) – 1/4 inch cell size core & carbon fiber composite skins, and Aerospace Commercial Grade (ACG) – 1 inch cell size core & carbon fiber composite skins. Although, sandwich panel has high stiffness and strength, its behavior under impact loading depends on mechanical properties of its constituents and the adhesive capability between two interfaces. Hence, it is highly responsive to slight changes in core material, type, and density, as well as, composite skin material, and fiber orientation. This paper details four failure modes of unidirectional carbon fiber composite skin with $[90/45]_2$ laminate configuration, and also comparative study of energy absorbing capabilities of two honeycomb cores with different strengths.

Nomenclature

T	=	Duration of impact (squash-up time)
L	=	Length of the bird
v_0	=	Initial impact velocity
ρ_0	=	Material initial density
ρ	=	Current density
U_0	=	Velocity of the bird material
U_s	=	Velocity of the shock in the bird material
U_{SP}	=	Shock velocity of projectile
U_{ST}	=	Shock velocity of target
P_c	=	Pressure at the center of the impact zone
c_0	=	Speed of sound in the material
s	=	Material constant
η	=	Nominal volumetric compressive strain $(1 - \rho_0/\rho)$
Γ_0	=	Grüneisen coefficient
E_m	=	Internal energy per unit mass
J	=	Jacobian determinant
t_i	=	Components of the traction vector
n_i	=	Components of the surface normal
D_i	=	Component of the enforced displacement vector
$\dot{\varepsilon}_{ij}$	=	Strain rate tensor
W_{ij}	=	Vorticity or Spin tensor
δx_i	=	Arbitrary test functions, can be interpreted as the virtual displacement field
dS	=	Area of a differential segment
a_i	=	Acceleration
$\bar{\varepsilon}_0^{pl}$	=	Initial value of equivalent plastic strain
$\dot{\varepsilon}^{pl}$	=	Equivalent plastic strain rate
$\bar{\varepsilon}_f^{pl}$	=	Strain at failure

$\bar{\varepsilon}^{pl}$	=	Plastic strain increment
x_i	=	Current position of a point
X_j	=	Location of the point in the original or reference frame
$\sigma_{ij,j}$	=	Cauchy stress
b_i	=	Applied body force per unit mass
v_i	=	Velocity in the current configuration
E_1	=	Young modulus (Longitudinal directional)
E_2	=	Young modulus (Transverse directional)
G_{12}	=	Shear modulus
v_{12}	=	Poisson ratio
S_{11}^+	=	Longitudinal tensile failure strength
S_{11}^-	=	Longitudinal compressive failure strength
S_{22}^+	=	Transverse tensile failure strength
S_{22}^-	=	Transverse compressive failure strength
S_{12}	=	Longitudinal shear failure strength
S_{23}	=	Transverse shear failure strength
F_f^+	=	Fiber failure index in tension
F_f^-	=	Fiber failure index in compression
F_m^+	=	Matrix failure index in tension
F_m^-	=	Matrix failure index in compressive
C_d	=	Elasticity matrix including damage

I. Introduction and Objective

As classic species of cellular materials, honeycombs have attracted a great deal of attention due to their outstanding properties, such as high relative stiffness and strength, good insulation, and lightweight. However, the sandwich structures are inherently susceptible to localized damage when subjected to localized transverse loads. Foreign Object Debris (FOD) is one of the common types of localized loads that may induce impact damage and result in reduction of static and/or fatigue strength of the sandwich structures. The impact behavior of a sandwich panel depends on many factors, such as mechanical properties of its constituents, skins, core, and adhesive capacity of the skin core interface. Regardless of extensive research on the sandwich structures, their impact behavior is still not fully understood [20].

The threat of bird strike event increases frequently due to rapidly growing air traffic and changes in the migration routes of the bird flocks [18]. The bird strike causes significant economic loss for all aviation, estimated at over $3 billion worldwide every year [19]. Many incidences were recorded in the past with the loss of aircrafts and even humans. Certification standards, which include the necessary level of tolerance to the bird strikes of aircraft structural parts, are established by U.S. Federal Aviation Administration (FAA) and European Aviation Safety Agency [EASA]. Generally, the bird strike testing on any structure part is done using gas-gun equipment that uses helium gas to shoot a real bird on a target. These empirical verifications, which cause damage of prototypes and the biological hazard of using real birds, can be costly and time consuming. The use of numerical methods serves as a powerful tool to support the certification process in order to minimize the cost of empirical testing.

The principle objective of the present work is to provide a numerical procedure that is capable of evaluating the residual compressive strength and the failure mechanisms of an aluminum-cored sandwich panels after a soft body impact. An accurate damage prediction of a composite honeycomb sandwich structure necessitates an appropriate modeling of the bird material, formulation methodology, and composite and honeycomb material.

II. Literature Search

As mentioned in the introduction that the impact behavior of honeycomb sandwich structures is still under investigation. G. Villanueva and W. Cantwell investigated a range of novel aluminum foam sandwich structure

under high impact velocity using nitrogen gas gun equipment. They used a 10 mm diameter metallic projectile to examine the various failure modes. Harte et al. noticed three failure modes, such as face sheet yield, core shearing, and indentation, of the sandwich composite structure under roller loading [14]. Similarly, McCormack et al. observed similar failure modes in addition to the face wrinkling in sandwich beams tested under three-point bending loading conditions [15]. The characteristics of the energy absorption capacity of a bare honeycomb cored under lateral crushing loads have been studied, both theoretically and experimentally, by Kunimoto et al. [16]. High velocity impact tests on the sandwich structures resulted in a number of different failure modes.

The earliest investigators, Wilbeck and Welsh, conducted a very comprehensive testing program to develop a substitute, synthetic bird model [1] [2]. In the past, for making a bird-proof design of aircraft components, it was a common practice to make and test the parts, then redesign and test them again. One example of this procedure is documented for the development of the bird-proof Dash 8 wing leading edge [8]. Without any doubts, this is certainly a time consuming and expensive method. Therefore, numerical methods are now adopted by aviation industries for the purpose of rapid and improved design optimization, ensuring that the very first full-scale bird strike certification test is successful. Outstanding work was done on bird strike impact numerical analysis by Smojver et al. [3] [4] [5]. McCarthy et al. carried out the analysis on Fiber Metal Laminates (FML), a family of material consisting of alternative plies of thin aluminum and fiber/epoxy with high specific strength, using Smooth Particle Hydrodynamics (SPH) method in PAM crash software [10]. Few works involve aerospace structures made of carbon-fiber reinforced polymer (CFRP) and Aramid fibers [11].

Earlier investigations in bird strike involved metallic projectiles-honeycomb structure targets, soft body projectiles-metallic/composite structures targets, and development of methodologies. The results from the metallic projectile-honeycomb structure target are not identical with the soft body projectile-honeycomb structure target. Hence, the detailed examination of the behavior of the composite sandwich structure is necessary to study its vulnerability under the soft body impact loading.

III. Bird Impact Theory

A. Background

Many aircrafts' exteriors are susceptible to collision with the birds, particularly during takeoff and landing phases. However, the high altitude impact cases had also been noted in the past. In order to assure the minimum safety standards in cases of the bird impacts, the international airworthiness standards require that the airplane tests must be conducted to demonstrate certain levels of capabilities, specified in terms of structural resistance and allowable degradation in flying qualities.

Various certification requirements are set by the certification authorities depending on the parts. Different weight birds are specified for the windshields, the wings, the empennage, and the engines. The final designs and acceptance of the bird resistant components are typically dependent on the testing. The typical method of the bird proofing an airplane is to build and test, then redesign and test again.

B. Bird Strike Certification

The bird strike tests are carried out in accordance with Federal Aviation Regulation (FAR) Parts 23, 25 and 33, as shown in Table 1. Earlier the tests used to involve a live chicken of an appropriate weight shooting against a structure that needs to be certified. However, for the simplicity, the sanitary, and the repeatability reasons, the synthetic bird of an appropriate size and weight is now used. The gas-gun type shooting cannon is used for the certification testing having 5-10 inches of diameter.

A typical windshield test program involves several birdshots at various locations of the windshield and the frame. In order to get the bird strike certification for the windshield and the frame, they have to show that the pilots should not be injured by the bird, the windshield fragments, the broken airframe, or the interior parts; and that the damaged structure and windshield should still hold the cabin pressure following the bird strike event. High-speed cameras, usually 10,000-20,000 frames per second, are placed inside and outside the cockpit to capture the details of any failure.

For the aircraft wing, the birdshots are done at the inboard and the outboard leading edges. The goal here is to show that the bird does not penetrate the wing leading edge, or even in case of penetration, it does not create any

critical damage to the wing front spar. The splitter plates, in the forms of triangular boxes, are often placed inside the leading edge skins to deflect the bird, and reinforce the leading edge structure.

The empennage is targeted at several spots along the leading edges of the vertical fin and the stabilizer, where vulnerabilities due to impacts are expected to be the highest. Like the wing, the typical goal is to prevent the front spar from critical damage to occur due to the bird strike. Here also, the splitter plates inside the skins are used to reinforce the leading edge structure.

For the engine, bird strike tests include the investigations of the impact effects on the engine operation as well as on the fan disk integrity. The engine operation test requires that the engine must continue to produce 75% of the thrust for 5 minutes after ingesting a small or medium size flock, as shown in Table 1. In Fan integrity test, the engine must not catch fire or disintegrate after being struck by a single 4 lb bird.

Table 1: Bird Strike Test Requirements [6]

FAR Section	Aircraft Components	Bird Strike Parameters		Performance Requirement
		Bird Mass	Aircraft Speed	
25.571 (e) (1)	General Structure	4 lb.	V_C @ sea level/ 0.85 V_C @ 8000 ft	Successful completion of flight
25.631	Empennage	8 lb.	V_C @ sea level	Continued safe flight and landing
25.775 (b)	Windshield	4 lb.	V_C @ sea level	Bird does not penetrate windshield
33.77, 25.571(e)(1)	Engine - Continued Operation	Up to 16 of 3 oz birds / Up to 8 of 1.5 lb birds	Not Specified	Engine must produce 75% of thrust for 5 minutes

C. Impact Theory

There are three major categories of the impact event: Elastic impact, Plastic impact, and Hydrodynamic impact. These impacts are categorized based on the impact velocity, and the level of the stresses generated in a projectile due to the impact.

The elastic impact is typically a low speed event, and the stresses generated due to collision are lower than the material yield stress. Therefore, the nature and duration of the impact depend on the elastic modulus and the elastic wave velocities of the materials. In case of a high impact speed, the produced stresses cause plastic deformation of the targeted material. For this event, the material strength is still a dominating factor, and hence such impact falls under the plastic impact category. Finally, for a very high impact velocity, the stresses generated by the deceleration of the projectile greatly excel the yield stress of the projectile material. This is the hydrodynamic regime, for which the projectile can be treated as a fluid.

1. Bird Impact Process

The bird impact process can be considered as the hydrodynamic impact. Peterson and Barber [24] summarized that the birds essentially behave like fluids during impacts; they do not bounce; and the impact duration is approximated from the bird squash-up time [24]. The squash-up time is given by

$$T = \frac{L}{v_0} \tag{1}$$

In these impact events, the projectiles' responses are determined by their masses and densities, but not by their materials' strengths. The bird impact process can be classified into four stages [25]: a) Initial impact phase, b) Shock Propagation, c) Steady State Flow, d) Pressure Decay Phase. Figure 1 shows the four stages of the soft body impact process.
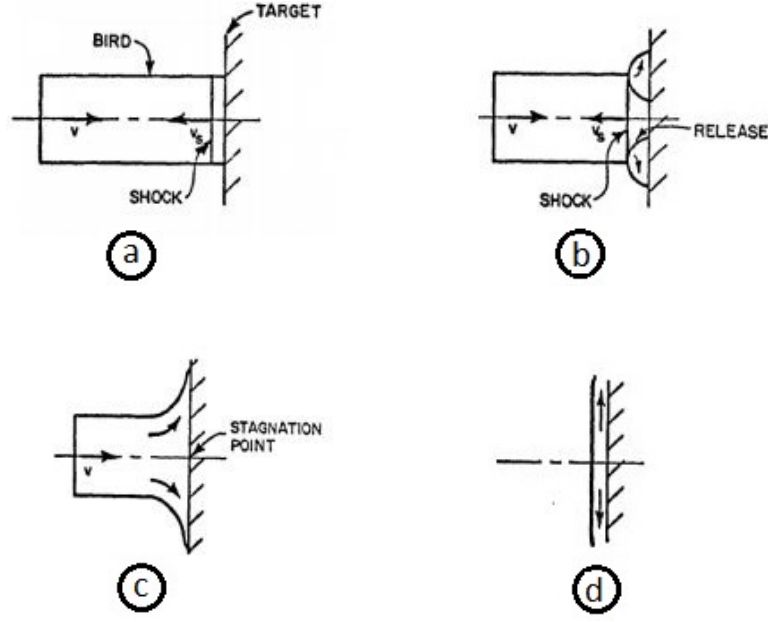
Figure 1: Bird impact process [25]

When a bird collides with an aircraft structure, the particles on the front surface of the bird are immediately brought to rest. Onset of high pressure from the first instant causes a shock wave to be generated at the bird/impacted structure's interface. This is the first phase of the impact theory that is shown in Figure 1(a). The pressure for a subsonic velocity is given by the Water Hammer equation, which is

$$P = \rho_0 c_0 U_0 \tag{2}$$

As the shock wave propagates, as shown in Figure 1(b), the impact velocity increases beyond a subsonic range, then a modified version of the water hammer equation is used to obtain the Hugoniot pressure. The modified water hammer equation is given by Equation (3).

$$P_H = \rho_0 U_s U_0 \tag{3}$$

Equations (2) and (3) are only applicable to the perfectly rigid targets. However, the compliant materials, such as aircraft transparency, absorb energies in the forms of kinetic energy, elastic strain energy, and plastic deformation. Hence, the modified version of the equation, given by Wilbeck and Rand[1], is given by Equation (4). Subscripts P and T represent a projectile and a target respectively.

$$P_c = \rho_P U_{SP} U_0 \left[\frac{\rho_T U_{ST}}{\rho_P U_{SP} + \rho_T U_{ST}} \right] \tag{4}$$

The duration of the bird strike event relies on the length of the bird. However, the shock compression of the layers of the particles is so rapid that it lasts only for few microseconds. In this work, the bird has been modeled as an incompressible fluid. The linear relationship between the shock and the particle velocities can be computed from the linear Mie-Grüneisen equation (Hugoniot equation).

$$U_s = sU_0 + c_0 \tag{5}$$

The final form of the pressure is given by following equation.

$$P = \frac{\rho_0 c_0^2 \eta}{(1 - s\eta)^2}\left(1 - \frac{\Gamma_0 \eta}{2}\right) + \Gamma_0 \rho_0 E_m \qquad (6)$$

Because of the very high-pressure gradient, the bird particles accelerate radially outward, and a release wave is formed. The function of the release wave is to relieve the radial pressures in the projectile. After several reflections of the release waves, the steady state condition is established as shown in Figure 1(c). The stagnation pressure on the impacted surface during this steady state is given by

$$P_s = k\rho_0 U_0^2 \qquad (7)$$

This stagnation pressure is independent of the bird shape. The steady state pressure is usually taken as 10-30% of the peak Hugoniot shock pressure at the center of the impacted region, based on experimental studies [26]. For an incompressible fluid, k = 0.5; but for most materials, the density increases with the pressure, and as a result, k may approach a value of 1.

IV.   Methods of Computation

Despite the extensive researches on a soft body impact, there is not any standardized method available to analyze the fluid-structure interaction impact problems. There are many methodologies present in different finite element codes. The selection of an appropriate method would often lead the solution closer to the experimental solution. It could be beneficial to couple different numerical solvers in order to leverage the advantages of each method.

There are currently four modeling methods available, such as Lagrangian, Eulerian, Coupled Lagrangian Eulerian (CEL), and Smooth Particle Hydrodynamics, which are being used for the impact damage analyses. Each methodology has its own strengths and weaknesses.

A. Lagrangian Formulation
In the Lagrangian formulation, the volume is divided into a large number of small geometries called elements. Mesh nodes are connected to a material by certain imaginary points called Integration points. The mesh follows the material, i.e. one material per element, during entire simulation. This formulation is generally used for solid materials. In the Lagrangian approach, the history dependent variables can easily be tracked. However, the major drawback of the Lagrangian formulation is that the large distortion of a part leads to hopeless mesh and element distortions causing inaccurate results and error termination of an analysis. The deformation of Lagrangian mesh [22] is shown in Figure 2 at different instants of time.

Figure 2: Lagrangian deformation for soft body impact simulation [22]

B. Eulerian Formulation
In the Eulerian formulation, a reference mesh is treated as a control volume, i.e. mesh remains fixed, and a material under study flows through the mesh. Since the mesh does not move, there is no possibility of mesh deformation, which is a major advantage.

This formulation is mostly applied to fluid applications. However, the Eulerian formulation requires more computations than the Lagrangian, which results in longer simulation time. In addition, it is very difficult to track the material interfaces, and the history of material variables. In Figure 3, the soft body impact simulation using the Eulerian formulation is shown at different instants of time.
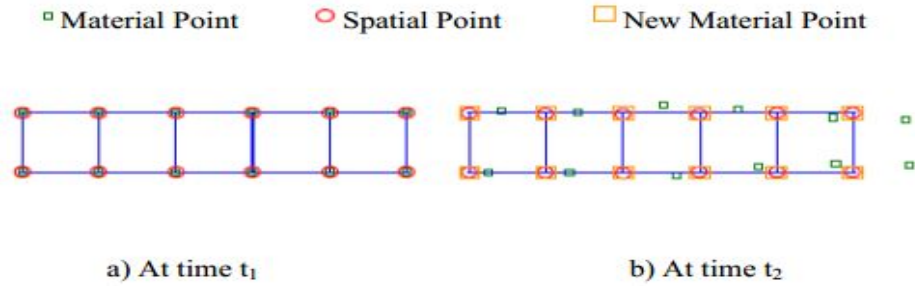
□ Material Point   ○ Spatial Point   □ New Material Point

a) At time t_1 b) At time t_2

Figure 3: Simulation in Eulerian formulation [23]

C. Coupled Eulerian Lagrangian Formulation (CEL)

The Coupled Eulerian Lagrangian formulation (CEL) is a combination of the Lagrangian, and the Eulerian formulation. The main objective of CEL method is to utilize the benefits of the Lagrangian, and the Eulerian formulations. For general Fluid-Structure problem, the Lagrangian mesh is used to discretize the structure, while the Eulerian mesh is used to discretize a fluid. The interface between the structure and the fluid can be represented using the boundary of the Lagrangian domain. On the other hand, the Eulerian mesh, which represents the fluid that may experience large deformation, has no problems regarding mesh, and element distortions. The only drawback of the CEL methodology is its longer computational time.

In Figure 4, a soft body impact simulation using the CEL formulation at different instants of time is represented. The CEL formulation can be considered similar to the Lagrangian formulation, and manual rezoning needs to be performed if entirely new mesh is required to continue the calculation. However, the accuracy of the CEL calculation is superior to the manually rezoned calculation. This is because the algorithm for the CEL calculation is second order accurate, while for the manual rezoning it is first order accurate.
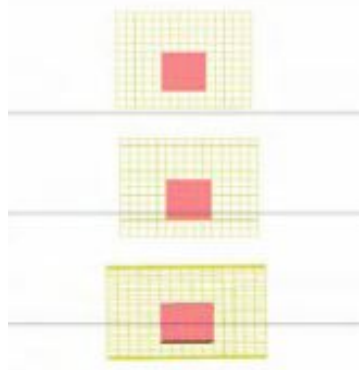

Figure 4: Soft body impact in CEL formulation [22]

D. Smooth Particle Hydrodynamics (SPH) Formulation

The Smooth Particle Hydrodynamics is a Lagrangian mesh-less technique for modeling fluid flow. The SPH integrates the hydrodynamic equations of motion on each particle in the Lagrangian formulation. The computations in the SPH are carried out by sorting technique. During simulation, the particle sorting is carried out after each cycle to determine the number of neighbors for each particle. The spatial distance, also known as smoothing length, varies in order to keep the same number of neighbors during simulation. In compression, the smoothing length gets small, while during tension it gets big. In the SPH, each particle has mass assigned to it. However, the interpolation method used in the SPH is very simple, and it will strongly be affected by a particle disorder. In addition, a boundary condition implementation is a hard task, and the fluid particles' penetrations into the boundaries must be avoided. Therefore, the integrity of this method is still under investigation. In Figure 5, the soft body impact simulation using the SPH formulation is shown at different instants of time.
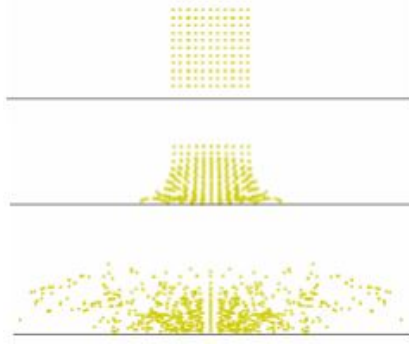
12

Figure 5: Soft body impact in SPH formulation [22]

V. Governing Equations

Simulating Bird's collision with a flight vehicle involves both kinematic nonlinearities, and material nonlinearities due to high strain rates, large deformations, and inelastic strains. In addition, inherent coupling between the impact loads and the response of the targeted structure raise complexity.

One of the pioneering works in the field of bird strike analysis was carried out by Wilbeck [1]. He proposed that the hydrodynamic theory could be applied to any projectile material during an impact even when the stresses in the projectile greatly exceed the projectile material strength. As a first step in the application of the hydrodynamic theory, Wilbeck decoupled the impact loads from the target response by assuming the targeted structure as rigid, and then included the effects of target flexibility. This method estimated the impact loading using 1-D shock relations in the shock regime, and by solving the 1-D compressible Bernoulli equation for the steady flow regime. However, due to the advanced computer technology today, the non-linear 3-D governing equations with contact conditions can be solved easily. The non-linear 3-D governing equations, such as conservation of mass, conservation of linear momentum, conservation of angular momentum, and conservation of energy, are described in the following section [27] [28] [29].

A. Conservation of Mass
The conservation of mass equation can be stated as

$$\rho J = \rho_0 \tag{8}$$

Jacobian determinant (J) is equal to the determinant of the deformation gradient F given by

$$J = det\left(F_{ij}\right) = \frac{\partial x_i}{\partial X_j} \tag{9}$$

In Equation (9), i and j range from 1 to 3 for 3-D. In a numerical computation procedure, the current density value ρ is computed based on the principle of conservation of mass, using the known initial density ρ_0.

B. Conservation of Linear Momentum
The conservation of linear momentum can be stated as Equation (10) under the appropriate boundary conditions. The dot above v_i represents the material time derivative.

$$\sigma_{ij,j} + \rho b_i = \rho \dot{v}_i \tag{10}$$

The application boundary conditions can take the following three forms:

1. Traction Boundary Condition
The traction boundary condition can be written as

13

$$\sigma_{ij}n_i = t_i \tag{11}$$

2. Displacement Boundary Condition
   The displacement boundary is formulated as follow:

$$x_i(X_i, t) = D_i(t) \tag{12}$$

3. Contact Boundary Condition
   At the contact surface, the displacement components of the two contacting surfaces must satisfy the constraint given Equation (13). Superscripts α and β refer to the two contacting surfaces.

$$\left(x_i^\alpha - x_i^\beta\right)n_i^\alpha \leq 0 \tag{13}$$

   In Equation (13), when the constraint is equality, the normal component of the tractions on the contacting surfaces must be equal and opposite. This condition can be written as

$$\sigma_{ij}^\alpha n_i^\alpha n_j^\alpha - \sigma_{ij}^\beta n_i^\beta n_j^\beta = 0 \tag{14}$$

C. Conservation of Angular Momentum
   In the absence of body couples, conservation of angular momentum simply states that the Cauchy stress tensor is symmetric, that is,

$$\sigma_{ij} = \sigma_{ji} \tag{15}$$

D. Conservation of Energy
   The conservation of energy equation is used to compute the internal energy (e), which is used in the equation of state to obtain the pressure-density relationship of a given material. The conservation of energy can be written as

$$\rho\dot{e} = \sigma_{ij}\dot{\varepsilon}_{ij} + \rho b_i v_i \tag{16}$$

   The strain rate is the same as the deformation rate D_{ij}. The deformation rate D_{ij} is obtained from the velocity gradient L_{ij}. The velocity gradient L_{ij} is defined as

$$L_{ij} = \frac{\partial v_i}{\partial x_j} \tag{17}$$

   The velocity gradient L_{ij} can be split into a symmetric component D_{ij} and a skew-symmetric component W_{ij} as follows:

$$D_{ij} = \frac{1}{2}\left(L_{ij} + L_{ji}\right) \tag{18}$$

$$W_{ij} = \frac{1}{2}\left(L_{ij} - L_{ji}\right) \tag{19}$$

E. Principle of Virtual Work

The finite element method uses the weak form of the momentum equation. In mechanics, the weak form is often referred to as the "principle of virtual work". The principle of virtual work is the weak form of the equation of conservation of linear momentum along with the traction, displacement, and contact discontinuity boundary conditions. The linear momentum equation along with the prescribed boundary conditions is called the generalized momentum balance. The weak form of the generalized momentum balance can be written as follows:

$$\int_V \left(\sigma_{ij,j} + \rho b_i - \rho \dot{v}_i \right) \delta x_i dV + \int_{\Gamma_t} \left(t_i - \sigma_{ij} n_j \right) \delta x_i dS - \int_{\Gamma_\alpha} \left(\sigma_{ij}^\alpha n_i^\alpha n_j^\alpha - \sigma_{ij}^\beta n_i^\beta n_j^\beta \right) \delta x_k^\alpha n_k^\alpha dS = 0 \tag{20}$$

δx_i must vanish everywhere except where the enforced displacement conditions exist. Using integration by parts, the first term in the above equation $\int_V \sigma_{ij,j} \delta x_i dV$ can be written as

$$\int_V \sigma_{ij,j} \delta x_i dV = \int_V \left[(\sigma_{ij,j} \delta x_i)_{,j} - \sigma_{ij} \delta x_{i,j} \right] dV \tag{21}$$

By applying the Gauss's divergence theorem, the first term on the right hand side of Equation (21) can be written as,

$$\int_V (\sigma_{ij,j} \delta x_i)_{,j} \, dV = \int_{\Gamma_t} \sigma_{ij} n_j \delta x_i dS + \int_{\Gamma_\alpha} \left(\sigma_{ij}^\alpha n_i^\alpha n_j^\alpha - \sigma_{ij}^\beta n_i^\beta n_j^\beta \right) \delta x_k^\alpha n_k^\alpha dS \tag{22}$$

Using Equation (22), the principle of virtual work now becomes

$$\delta \pi = \int_V \sigma_{ij} \delta x_{i,j} dV + \int_V \rho a_i \delta x_i dV - \int_V \rho b_i \delta x_i dV - \int_{\Gamma_t} t_i \delta x_i dS = 0 \tag{23}$$

F. CEL Equations

The Coupled Eulerian Lagrangian (CEL) formulation contains both, the Lagrangian and Eulerian, equations as subsets. The velocity of the material is u, the velocity of the reference coordinates is v, and their difference, u-v, is denoted as w. The Jacobian, J', is the relative differential volume between the reference and spatial coordinates.

$$\frac{\partial J'}{\partial t} = J' \frac{\partial v_i}{\partial x_i} \tag{24}$$

The material time derivative can be expressed in terms of both the spatial and reference coordinates, where f^r means that f is expressed as a function of the reference coordinates.

$$\dot{f} = \frac{\partial f}{\partial t} + u_i \frac{\partial f}{\partial x_i} \tag{25a}$$

$$\dot{f} = \frac{\partial f^r}{\partial t} + (u_i - v_i) \frac{\partial f}{\partial x_i} \tag{25b}$$

The CEL equations are derived by substituting Equation (25) into the equations of conservation of mass, momentum, and energy, however they are not in conservation form.

$$\frac{\partial \rho^r}{\partial t} = -\rho \frac{\partial u_i}{\partial x_i} - w_i \frac{\partial \rho}{\partial x_i} \tag{26a}$$

15

$$\rho \frac{\partial u_i^r}{\partial t} = (\sigma_{ij,j} + \rho b_i) - \rho w_i \frac{\partial u_i}{\partial x_i} \tag{26b}$$

$$\rho \frac{\partial e^r}{\partial t} = (\sigma_{ij} u_{i,j} + \rho b_i u_i) - \rho w_i \frac{\partial e}{\partial x_j} \tag{26c}$$

To put them into conservation form, an additional identity is derived by multiplying Equation (26a) by J', multiplying Equation (24) by ρ, and adding them.

$$\frac{\partial J' \rho}{\partial t} = -J' \frac{\partial \rho w_i}{\partial x_i} \tag{27}$$

After multiplying Equation (26) by f, Equation (25b) by $\rho J'$, and arranging terms, the CEL equation for f is written in its general form. The first term on the right hand side of Equation (28) is the source term for f, and the second term, the transport of f.

$$\frac{\partial (J' \rho f)}{\partial t} = J' \rho \dot{f} - J' \frac{\partial \rho f w_i}{\partial x_i} \tag{28}$$

The conservation form of the CEL equations is obtained by substituting the Lagrangian equations into Equation (28).

$$\frac{\partial \rho J'}{\partial t} = -J' \frac{\partial \rho w_i}{\partial x_i} \tag{29a}$$

$$\frac{\partial \rho J' u_i}{\partial t} = J'(\sigma_{ij,j} + \rho b_i) - J' \frac{\partial \rho u_i w_j}{\partial x_j} \tag{29b}$$

$$\frac{\partial \rho J' e}{\partial t} = J'(\sigma_{ij} u_{i,j} + \rho b_i u_i) - J' \frac{\partial \rho e w_j}{\partial x_j} \tag{29c}$$

When w is zero, J' is one, and the Lagrangian equations are recovered from Equation (29). If the reference coordinates are the current spatial coordinates, w is v, J' is again one, and the Eulerian equations are recovered.

VI.   Honeycomb Structure

Honeycomb structures are finding increasing use in aerospace, automotive, and marine industries because of their relative advantages over other structural materials in terms of improved stability, high stiffness to weight and strength to weight ratios. They provide an efficient solution to increase bending stiffness without significant increase in the structural weight. The honeycomb structure can carry both in-plane and out-of-plane loads and remains stable under compression without a significant weight penalty.

While the preliminary design of aircraft sandwich structures have been investigated extensively in the past years, there is a lack of understanding of a soft body impact-damage mechanism, and the effect of such damage on structural performance. The presence of highly complex and transient dynamic failure modes in such materials and the inaccessibility of internal damage to real-time monitoring have limited experimental studies to the final impact damage characteristics of the failure and residual strengths.

Sandwich constructions are being considered for applications to aircraft primary structures, where durability and damage tolerance are the primary considerations. Therefore, understanding the adverse effects of in-service impact events has become vital. Certification authorities, such as Federal Aviation Administration (FAA), and European Aviation Safety Agency (EASA), require that exposed aircraft components must be tested to prove their capability to withstand such impact without suffering any critical damage.

The impact may induce overall or localized damage in sandwich structures. The failure characteristics of sandwich structures are significantly different from conventional laminated structures, and are strongly dependent on the core and skin materials, and their thicknesses. The localized damage is usually confined to the top facing, the core-top facing interface, and the core material. The bottom skin is generally left undamaged. In particular, permanent indentation in the impacted face-sheet accompanies with localized core crushing beneath and around the impact site. The facing skin will typically rebound to some degree after the impact event; therefore, the profile of the residual face-sheet indentation does not necessarily correspond to that of the underlying crushed core. Depending on the size and mass of the impactor and impact energy, various damage modes that may develop failure are: (a) delamination in the impacted face-sheet, (b) skin-core debonding, (c) core crushing and shear, (d) matrix cracking, (e) fiber breakage in the facings, and (f) core buckling [34].

A. Sandwich Construction

Honeycomb sandwich panel has a middle layer (core) in honeybee comb shape to allow the minimization of weight and material cost. It is made by layering a honeycomb material between two thin layers. A film of an adhesive material is used between face skins and honeycomb core to allow them to stick together. The construction of the sandwich panel is shown in Figure 6. The panel face skins carry tensile and compressive loads, and the honeycomb core carries transverse stresses. In a highly loaded panel, the transverse stresses may approach the strength of the honeycomb core. Thus, it is important to use the correct properties when designing a panel.
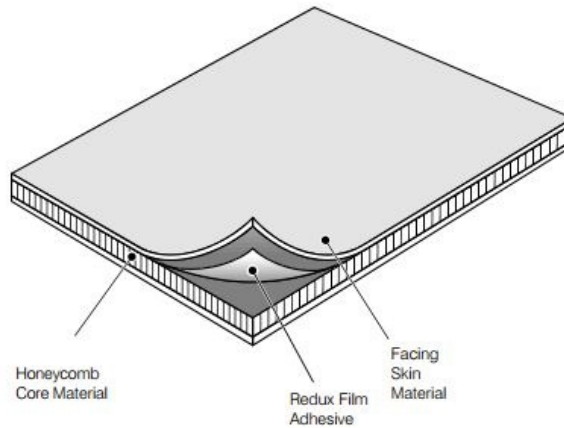

Figure 6: Sandwich Panel [35]

B. Honeycomb Core

The honeycomb core is manufactured by two methods, Expansion Process, and Corrugated Process. The corrugated process of the honeycomb manufacture is commonly used to produce products in a higher density range [36]. Figure 7 shows a standard hexagonal honeycomb that is widely used for many aerospace applications. In the honeycomb core, the corrugated sheets are attached to each other with help of adhesive materials, and a point of attachment is called node bond. These corrugated sheets are also known as ribbons. The

Figure 7: Honeycomb Core and its Terminology [35]

honeycomb core is classified by a shape made by two adjacent corrugated sheets (hexagonal in Figure 7). A cell size is measured between two opposite sides of a polygon made by corrugated sheets, and a transverse dimension of the corrugated sheet is defined as a thickness of the core. The density of the core depends on the cell size. Larger the cell size, lower will be the density of the core. Vice-a-versa, smaller the cell size, higher will be the density of the core. The large cell size is the lower cost option, but provides lesser bonding area that may result in a dimpled outer surface of the sandwich. While, the small cell size gives improved surface appearance by providing a greater bonding area with slightly higher cost.
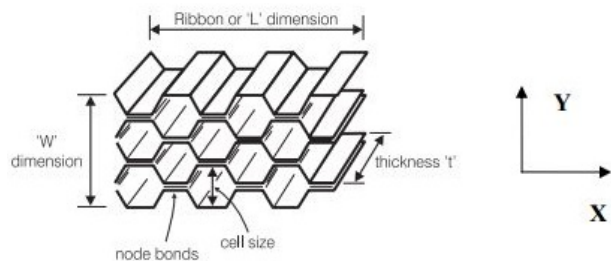
The behavior of the honeycomb core is orthotropic; hence, the panels react differently depending on the orientation of the structure. Therefore, it is necessary to distinguish between the directions of symmetry. The material directions used for the core characterization are defined in Figure 7. The transverse properties of the core are dependent on the ribbon (L) direction. When the honeycomb cells are compressed in W-direction, because of the hexagonal shape of the cell, the inclined edges of the hexagon collapse due to bending about the symmetric X-axis. However, when the compression load is applied parallel to the ribbon (L) direction, the horizontal edges of the cell provide better compressive resistance than inclined edges. Therefore, the 'L' or ribbon direction is the strongest and the stiffest direction, the weakest direction is at 60˚ from the L-direction (in the case of a regular hexagon), and the most compliant direction is the 'W' or transverse-to-ribbon direction [37].

The out-of-plane (L-T plane or W-T plane) compressive properties of honeycomb, such as stiffness and strength, are important in structural applications. The impact performance is mainly dependent on transverse compressive properties. Honeycombs are particularly strong in the out-of-plane direction. Because, when they are loaded in this direction, the cell walls that are aligned with the load expand or compress rather than undergoing bending.

C. Energy Absorption Mechanism of the Honeycomb Core

Honeycombs are widely used as energy absorption devices in aircraft, automobiles etc. Honeycomb core is typically characterized for energy absorption in the T-direction, which represents its strong axis. The energy absorption is high for loading parallel to T-direction. The load-deflection curve shown in Figure 8 is obtained by compressing the honeycomb core in the out-of-plane direction. The material behavior can be characterized by various stages as illustrated on the plot. The honeycomb behavior under transverse compression is characterized by an initial linear region up to a maximum load that corresponds to an initiation of a failure in the core walls. The failure modes depend on the core wall material, thickness, and cell geometry. The failure modes include cell wall yielding, or cell wall fracture due to localized buckling modes. The load subsequently drops to a certain level at which progressive failure occurs. The progressive failure involves crushing of the core where the cell walls fold in an accordion manner. The progressive crushing occurs at an almost uniform load until the densification of crushed material occurs resulting in rapid increase of compressive load. The crushing of the core at a constant load level results in energy absorption, which can be calculated by measuring an area under the load-deflection curve.
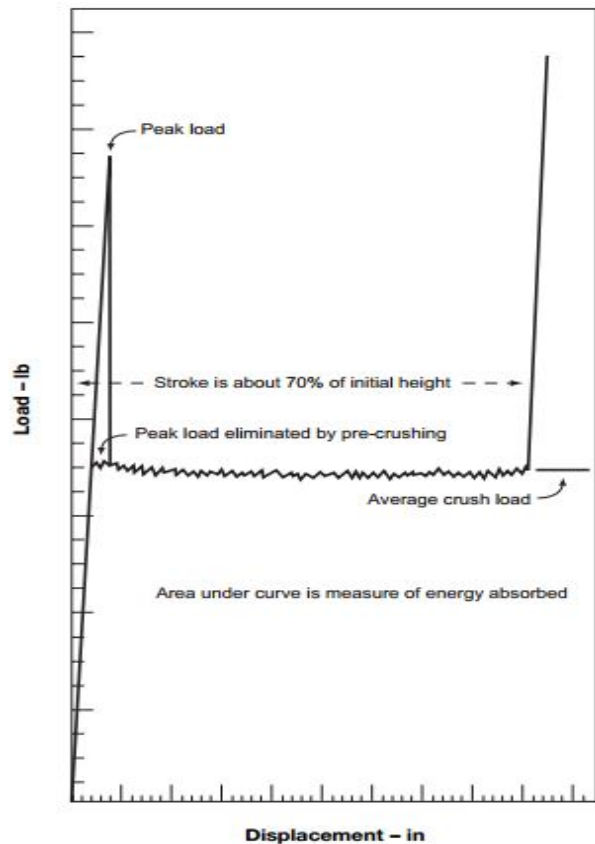

Figure 8: Load-Displacement Curve of Out-of-Plane Compression of Honeycomb Core [36]

VII. Numerical Model

The impact behavior of the sandwich leading edge with spar was implemented in Abaqus/Explicit transient finite element code. A wing leading edge is made of unidirectional carbon fiber face skins and an aluminum hexagonal core. Both face skins have four layers of AS4 carbon fibers and 8552 epoxy resin ply in [90/45/45/90] laminate configuration. Each ply is 0.125 mm thick, making each face skin 0.5 mm thick. The core is a 3003 aluminum hexagonal honeycomb with 6 mm thickness. The front spar is made of Al 7075.

The leading edge numerical discretization is shown in Figure 9. For the numerical analysis, the small portion of the leading edge of span 1 m, and chord 0.85 m is analyzed. For the finite element model, numerous joints between the elements, e.g. rivets, are neglected, thus avoiding unnecessary nonlinearities and contact surfaces. This is justified by the need to make the structure as simple as possible, but at the same time enabling correct simulation of the load transfer between the components, within the reasonable computational cost. The thicknesses of top and bottom faces are relatively smaller than other two principle dimensions. Therefore, the top and bottom faces of a sandwich structure are meshed with conventional shell elements (S4R) giving only 4 nodes for the computation of each element, which is computationally faster than continuum shell elements (SC8R) with 8 nodes for each element. The sandwich core is modeled using first order solid elements (C3D8R). The conventional shell (S4R) and solid (C3D8R) elements have only translational degrees of freedom. Therefore, the need of kinematic constraint can be eliminated by sharing the same interface nodes for coupling of face layer and core elements. The kinematic constraint has been achieved by imposing tie surface based constraint at the interface nodes. The front spar is meshed using solid element (C3D8R). There are total 35000 conventional shell elements (S4R) and 17600 solid elements (C3D8R). The total numbers of elements for the whole model is 235644.
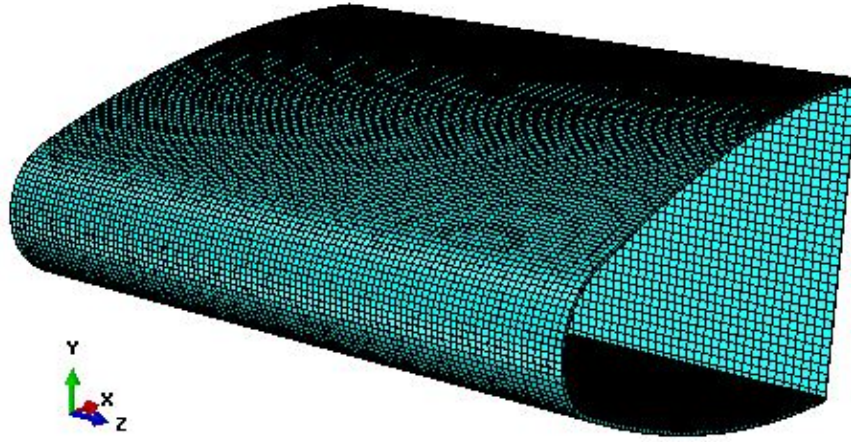

Figure 9: Wing Leading Edge Finite Element Mesh

A. Composite Material and Failure Modeling

In the present work, the composite failure and damage modeling has been achieved by Abaqus built-in Hashin's progressive failure criterion. The Hashin failure criterion is used to evaluate failure in an individual composite ply [42]. This model predicts intra-laminar damage modes such as fiber failure in tension and compression, and matrix cracking in tension and compression. The failure criterion is expressed in terms of the planner stresses σ_{ij}, the fiber direction and transverse direction strengths, and the allowable shear strength. Mechanical properties of unidirectional CFRP layers are listed in Table 2.

Table 2: Mechanical Properties of CFRP AS4/8552 [41]

ρ (kg/m^3)	E_1 (GPa)	E_2 (GPa)	G_{12} (GPa)	ν_{12}	S_{11}^+ (MPa)	S_{11}^- (MPa)	S_{22}^+ (MPa)	S_{22}^- (MPa)	S_{12} (MPa)
1580	107.3	10.75	5.58	0.3	2068	1740	67.08	355	74

Fiber failure in tension and compression is considered to occur independently of the other stress components in the Hashin failure criterion. The fiber failure index is defined as,

If $\sigma_{11} \geq 0$, then the Tensile Fiber Failure Criterion is:

$$F_f^+ = \left(\frac{\sigma_{11}}{S_{11}^+}\right)^2 + \alpha \left(\frac{\sigma_{11}}{S_{12}}\right)^2 \geq 1.0 \tag{30}$$

If $\sigma_{11} < 0$, then the Compressive Fiber Failure Criterion is:

$$F_f^- = \left(\frac{\sigma_{11}}{S_{11}^-}\right)^2 \geq 1.0 \tag{31}$$

Similarly, for the matrix failure in tension and compressive, the matrix failure index is given by Equation (32) and (33) respectively.

If $\sigma_{22} \geq 0$, then the Tensile Matrix Failure Criterion is:

$$F_m^+ = \left(\frac{\sigma_{22}}{S_{22}^+}\right)^2 + \alpha \left(\frac{\sigma_{12}}{S_{12}}\right)^2 \geq 1.0 \tag{32}$$

If $\sigma_{22} < 0$, then the Compressive Matrix Failure Criterion is:

$$F_m^- = \left(\frac{\sigma_{22}}{2S_{23}}\right)^2 + \left[\left(\frac{S_{22}^-}{2S_{23}}\right)^2 - 1\right]\frac{\sigma_{22}}{S_{22}^-} + \left(\frac{\sigma_{12}}{S_{12}}\right)^2 \geq 1.0 \tag{33}$$

The user-defined parameter (α) in Hashin failure criteria determines the contribution of the longitudinal shear stress to fiber tensile failure. The allowable range is between 0 to 1. When there is no test data available to correlate the failure envelop, it is recommended to set the parameter to 0. The material properties are degraded based upon the damage mode in which damage parameters modify the initial undamaged elasticity matrix. Fiber (d_f), matrix (d_m), and shear (d_s) damage parameters reflect the current state of damage, having values ranging 0 to 1 for undamaged and completely degraded material, respectively. The damaged elasticity matrix has the form as below:

$$C_d = \frac{1}{D}\begin{bmatrix} (1-d_f)E_1 & (1-d_f)(1-d_m)\nu_{21}E_1 & 0 \\ (1-d_f)(1-d_m)\nu_{12}E_2 & (1-d_m)E_2 & 0 \\ 0 & 0 & (1-d_s)G_{12}D \end{bmatrix} \tag{34}$$

Where $D = 1 - (1-d_f)(1-d_m)\nu_{12}\nu_{21}$. E_1, E_2, G_{12}, ν_{12}, and ν_{21} are unidirectional ply material properties.
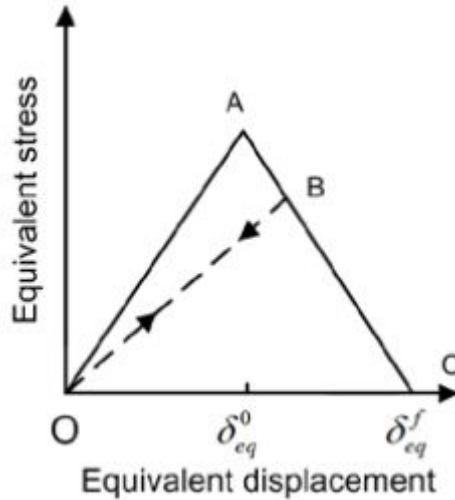

Figure 10: Equivalent Stress-Displacement Diagram [4]

In degradation of the CFRP material, Abaqus uses a constitutive law expressed as a stress-equivalent displacement relation. The stress vs. displacement chart is shown in Figure 10. The elastic behavior of the material is represented by the positive slope (OA) of the stress-displacement curve. When Hashin's damage initiation criterion is reached, damage parameters modify the stiffness matrix and degrade the material properties. This part of stress-equivalent displacement curve is represented by the negative slope curve (AC). At last, path BO on the stress-displacement curve represents the unloading and reloading from a partially damaged state. The area of the triangle OAC is equal to the energy dissipated due to damage, which is generally obtained from the experiment. For this model, the dissipated fracture energy for all four modes, such as, longitudinal tensile and compressive fracture energies, transverse tensile and compressive fracture energies, is taken as 738 J/m^2 [38]. After damage initiation, the damage parameter of a particular failure mode is given by Equation (34).

$$d = \frac{\delta_{eq}^{f}(\delta_{eq} - \delta_{eq}^{0})}{\delta_{eq}(\delta_{eq}^{f} - \delta_{eq}^{0})} \tag{35}$$

The graphical presentation of Equation (35) is shown in Figure 11. An element is removed from the mesh when all material points reach the critical degradation value.
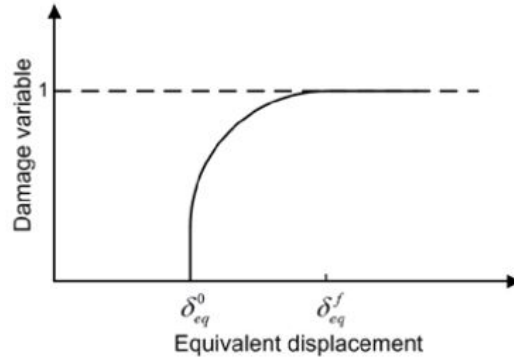

Figure 11: Damage Variable as a function of Equivalent Displacement [4]

B. Material modeling of honeycomb core

Characteristic behavior of Aluminum honeycomb cores under compressive loads is shown in Figure 12. The honeycomb core behaves elastically at low strains ranging from 0.5 to 5%. Once the stress reaches to its yield strength, the progressive core crushing starts at nearly constant stress level called the plateau stress (σ_{pl}). At a strain value of about 85%, the stress increases drastically due to mutual pressing of the cell walls.
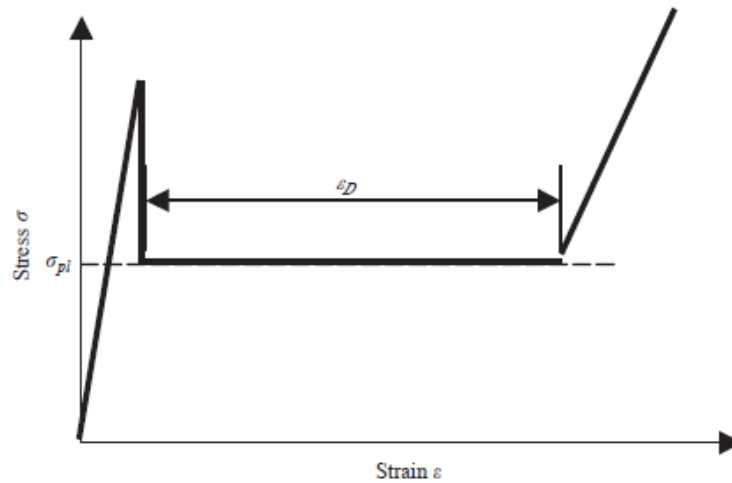

Figure 12: Schematic Stress-Strain Curve for Honeycomb [39]

21

In Abaqus, the crushable foam material model is used to model the aluminum foam. This is a very simple material model, which allows for a description of the foam behavior through the input of a stress versus volumetric strain curve. The stress versus strain behavior is depicted in Figure 12. In this model, the foam is assumed isotropic and crushed one-dimensionally with a Poisson's ratio that is essentially zero. The model transforms the stressed into the principal stress space where the yielding function is defined, and yielding is governed by the largest principal stress. The principal stresses are compared with the yielding stress in compression and tension. If the actual stress component is compressive, then the stress has to be compared with a yield stress from a given volumetric strain-hardening function specified by the user $Y_c = Y_c^0 + H(ev)$. On the contrary, when the considered principal stress component is tensile, the comparison with the yield surface is made with regard to a constant tensile cutoff stress, also known as crush strength. Hence, the hardening function in tension is similar to that of an elastic, perfectly plastic material. The shear failure criterion is used to remove core elements from the mesh when an equivalent plastic strain of 5% is reached. The shear failure criterion, which is highly recommended for dynamic problems, is defined to model the failure of metallic structures. The shear failure criterion is given by Equation (34), which is based on the accumulated equivalent plastic strain [33].

$$\bar{\varepsilon}^{pl} = \bar{\varepsilon}_0^{pl} + \int_0^t \sqrt{\frac{2}{3} \dot{\varepsilon}^{pl} : \dot{\varepsilon}^{pl}} \, dt \tag{36}$$

Approximately, an element fails when the damage parameter (ω) exceeds the value of 1. The damage parameter is calculated as

$$\omega = \frac{\bar{\varepsilon}_0^{pl} + \sum \Delta \bar{\varepsilon}^{pl}}{\bar{\varepsilon}_f^{pl}} \tag{37}$$

Mechanical properties of the honeycomb core are listed in Table 3.

Table 3: Aluminum Commercial Grade (ACG) for 3000 Series Alloy [36]

Honeycomb Designation Material – Cell Size	Nominal Density (pcf)	σ_{comp} (psi)	σ_{crush} (psi)	E_{comp} (ksi)
ACG-1/4	4.8	660	245	148
ACG-1	1.3	85	25	16

C. Coupled Eulerian Lagrangian (CEL) bird model

In CEL analysis of a bird impact, the Eulerian space through which the Eulerian material flows and collides with the Lagrangian structure is represented by a stationary cube. Meshing is simplified in the CEL approach, as there is no need to mesh the soft projectile (Bird). The Eulerian space is meshed with EC3D8R element, the only mesh type available in Abaqus for the Eulerian problems. The bird material may be assigned completely or partially to these elements, while the void material is automatically assigned to the rest of the Eulerian grids [33]. The Eulerian Volume Fraction (EVF) tool, available in the Load module, is used to track the bird material as it flows through the mesh. The EVF represents the ratio by which each Eulerian element is filled with a material. The elements filled with a material have EVF of one, while the void elements have EVF of zero. The Eulerian domain must be sufficiently large to encompass the bird and the Lagrangian target plate even after the impact, as the loss of the bird material would lead to faulty results because of loss of the kinetic energy. In the CEL method, because the mesh does not move, the mesh deformations do not occur and the explicit time step is not influenced. Since, there is no need to mesh a bird in the CEL method, the stability problems due to excessive element deformations do not occur.

1. Bird Geometry

The bird geometry is represented as a simple primitive geometry of a cylinder with hemispherical ends as this geometry resembles the pressure time histories of real birds during impact tests [30]. The bird characteristics, such as diameter, cylindrical length, and density, are obtained by the empirical formulas as suggested in Ref. [31].
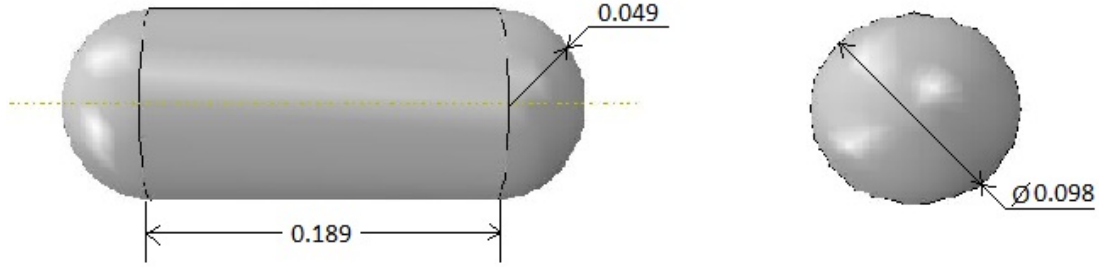
$$Bird\ Mass = 4\ lb = 1.81\ kg$$

$$Density = 959 - 63 * log_{10}(Bird\ Mass) \tag{38}$$
$$= 942.7\ kg/m^3$$

$$Diameter = 0.0804 * Bird\ Mass^{0.335} \tag{39}$$
$$= 0.098\ m$$

$$Cylinder\ Length = 4 * \left(\frac{Bird\ Mass}{\pi * Density * Diameter^2} - \frac{Diameter}{6}\right) \tag{40}$$
$$= 0.189\ m$$

$$Total\ Length = Cylinder\ Length + Diameter \tag{41}$$
$$= 0.287\ m$$

The geometry of the bird model is shown in Figure 13.

Figure 13: Bird geometry (All dimensions are in meters)

2. Bird Material

The bird material is substituted by an equal mass of water, as birds mostly consist of water and air trapped in the bones and the lungs. The bird is modeled with the Mie-Grueneisen (Us-Up) equation of state (EOS) material model to capture the hydrodynamic response of the bird. To define the EOS material in Abaqus, only four material properties, such as reference density (ρ_0), Grueneisen coefficient (Γ_0), speed of sound (c_0), and material constant (s), need to be specified in Equation (6). For water, these properties are $c_0 = 1480$ m/s, $\Gamma_0 = 0$, and s = 0^{17}, while reference density (ρ_0) is $942.7\ kg/m^3$, as calculated above.

VIII. Numerical model validation

A. CEL bird model validation

For the verification of the CEL bird model. The bird is fired against an Aluminum alloy (AL 6061 T-6) flat plate with dimensions of 550 x 550 x 6.35mm at a speed of 150 m/s. The flat plate is fixed at all ends. The analyses are carried out with both methods: the Lagrangian, and the Coupled Eulerian Lagragian. The Lagrangian modeling method is a standard approach for the most of the structural finite element analyses with the nodes of the Lagrangian mesh being associated to the material, and therefore following the material under a motion and a deformation. In this method, both, the bird and the aluminum plate, are meshed. The bird finite element model is idealized with the Lagrangian solid element (C3D8R) that enforces viscous hourglass and distortion control to resist excessive element distortions. Then, the results obtained from both methods are compared with the experimental test data [2].

The target plate material is defined by giving its density, isotropic elastic and plastic behavior, and isotropic damage evaluation and initiation. Mechanical properties of the Aluminum 6061-T6 is taken from Ref. [32], also listed in Table 4.

**Table 4: Mechanical properties of Aluminum 6061-T6 [32]**

ρ (kg/m^3)	E (GPa)	v	σ_y (MPa)	ε_{fail}
2712	68.29	0.33	248	0.15

The Aluminum plate finite element model is made under the shell definition because of its relatively small thickness. The conventional shell element (S4R) is used for meshing the aluminum plate. The strain rate effect on the plate material's mechanical properties is disregarded by the fact that the low material strength of the bird might not directly affect the metallic structures. The shear failure criterion as described before is used to model the aluminum material failure.
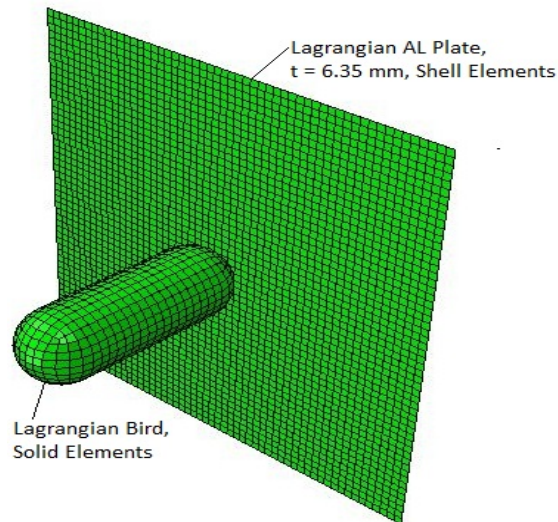
Figure 14: Bird model setup (Lagrangian Formulation)

The aluminum plate is discretized by 3025 shell elements (S4R), while the bird has 1844 solid elements (C3D8R) in Lagrangian formulation, as shown in Figure 14.
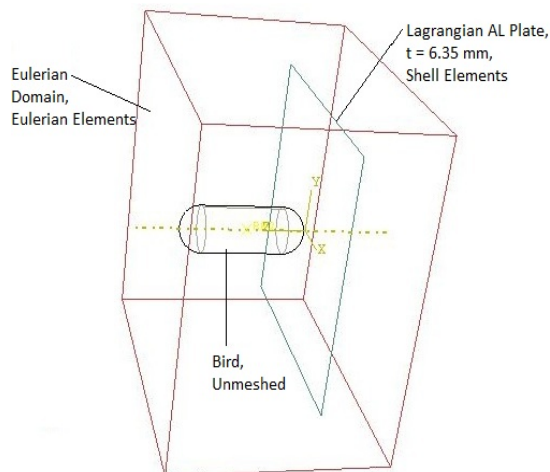
Figure 15: Bird model setup (CEL Formulation)

The placement of the Aluminum plate and the bird model in Eulerian domain is shown in Figure 15. There are total 245000 Eulerian elements (EC3D8R), and 2500 shell elements (S4R).

The deflection contours of the aluminum plate due to bird strike are shown in Figure 16 & 17. The maximum deflection at the center of the impacted plate in the gas-gun experiment at the impact speed of 150 m/s is 41.3 mm

[2]. Smojver analyses measured the deflections of 40.7 mm and 38.54 mm in the Lagrangian and CEL formulation respectively [3] [4]. The current numerical analyses measure maximum deflections of 41.84 mm for the Lagrangian, while 39.40 mm for the CEL bird model.
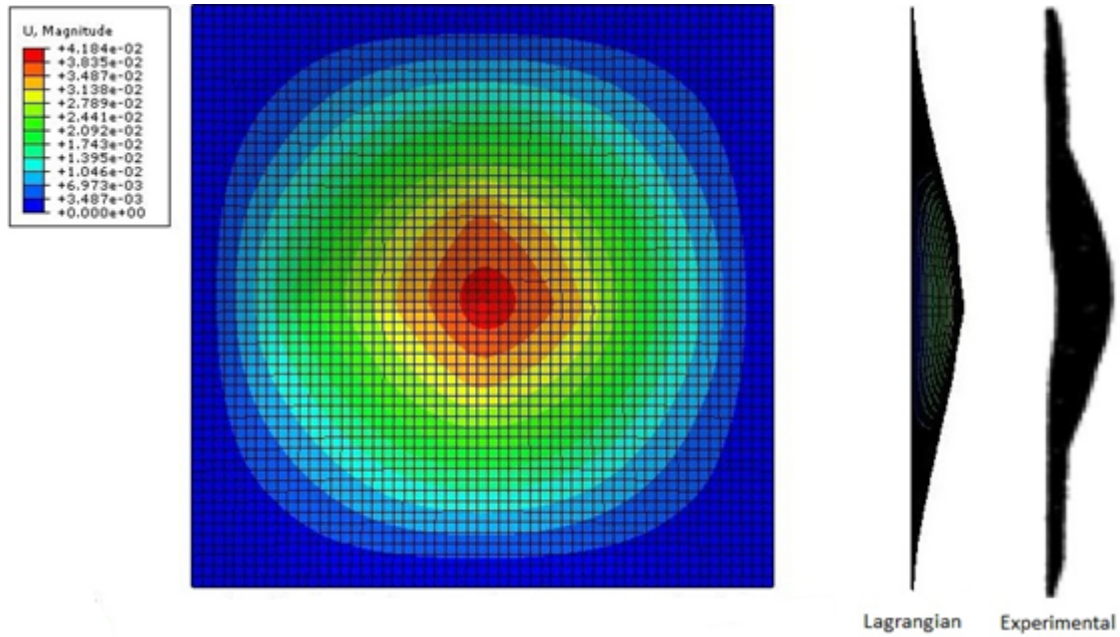

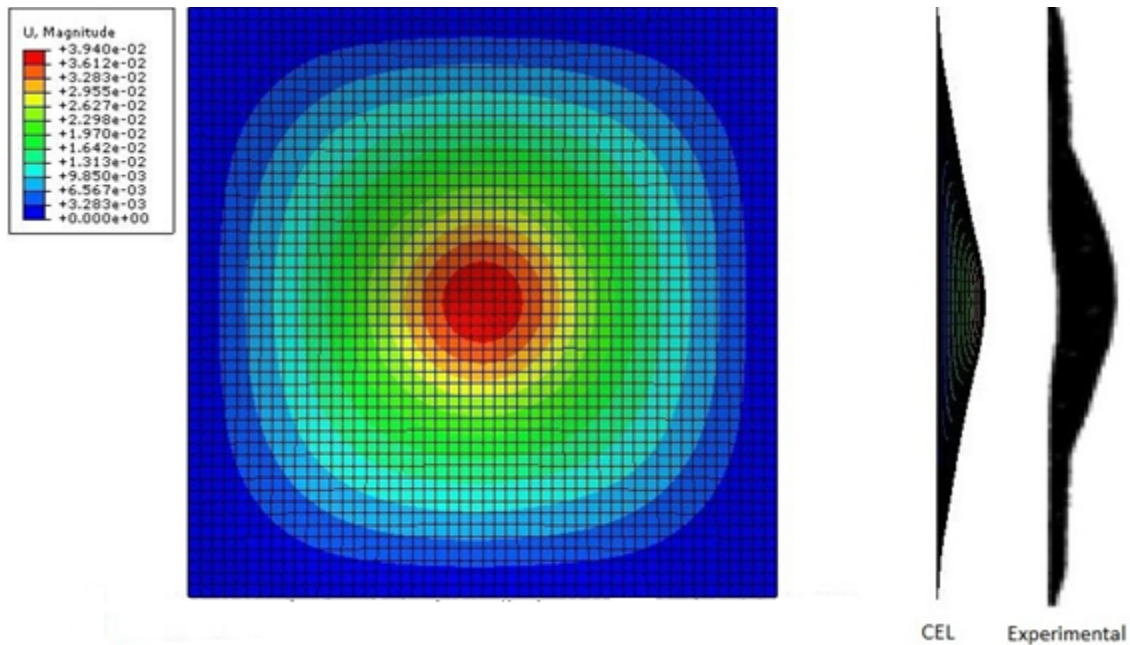**Figure 16: Displacement contours of Aluminum plate (Lagrangian Method), at V = 150 m/s**

Figure 17: Displacement contours of Aluminum plate (CEL Method), at V = 150 m/s

Although, the result for the Lagrangian bird model is close to the value obtained by the gas-gun tests, the plate deflection distribution and its deformed shape after an impact are more realistic for the CEL model. Figure 16 illustrates that the slope of the deflected region near the center is very high for the Lagrangian impactor, which does

not resemble with the experimental result. While in case of the CEL bird model, the impact forces are uniformly distributed, and the deformed plate shape matches the experimental result as shown in Figure 17.

As discussed earlier, the bird impact phenomenon has been divided into four distinct stages: Initial impact, shock propagation, steady state flow, and pressure decay phase. Figure 18 (a), (b), (c), and (d) show the four stages of the bird impact event, namely, initial impact, shock propagation, steady state flow, and pressure decay, respectively. The colors represent the displacement contours at varied time intervals in CEL bird model formulation.
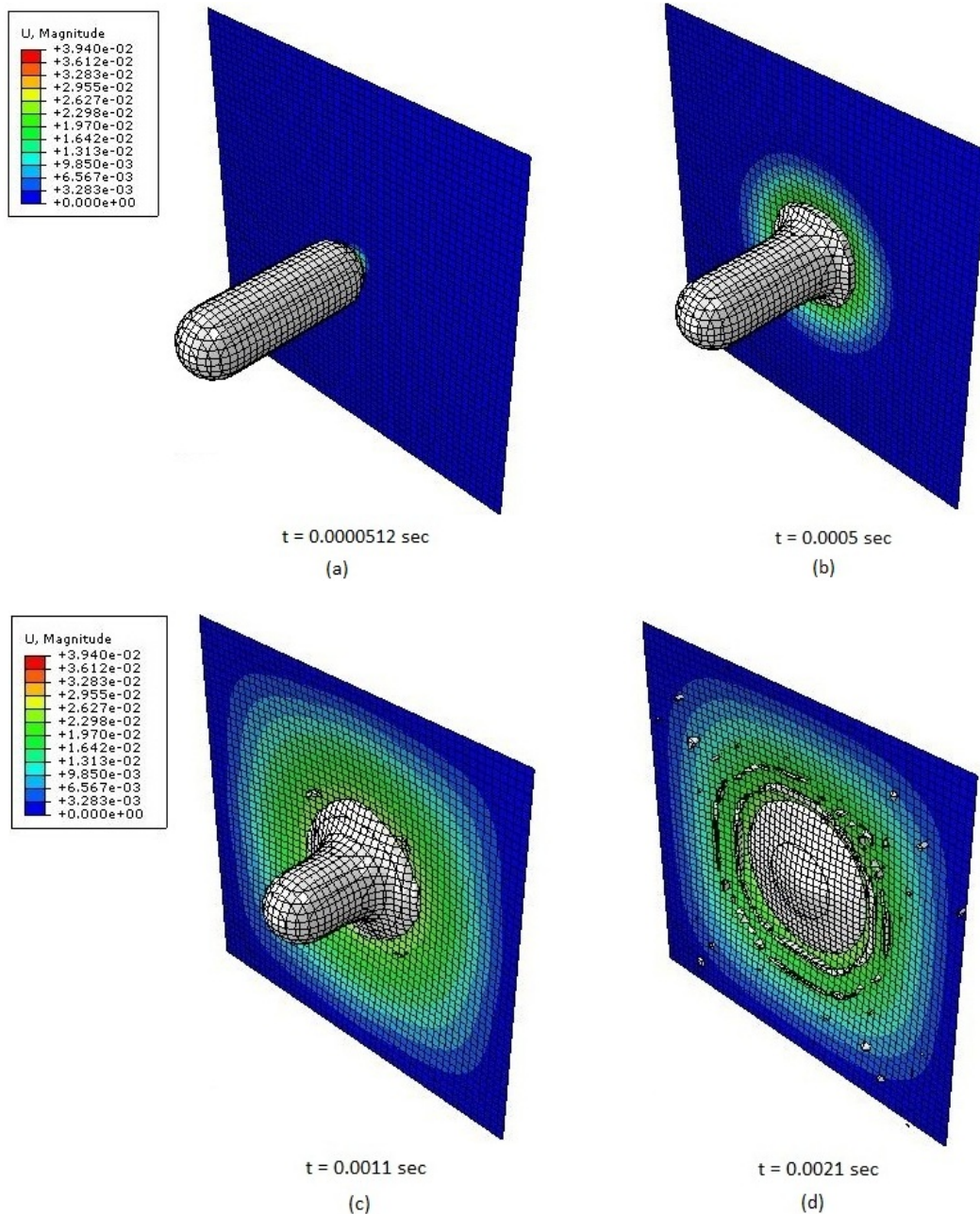
**Figure 18: Bird Impact at various time interval, at V = 150 m/s**

Figure 19 shows a chart of displacement in meters versus time. Approximately, the maximum deflection of 39.40 mm has been occurred at 0.0018 sec after the impact.
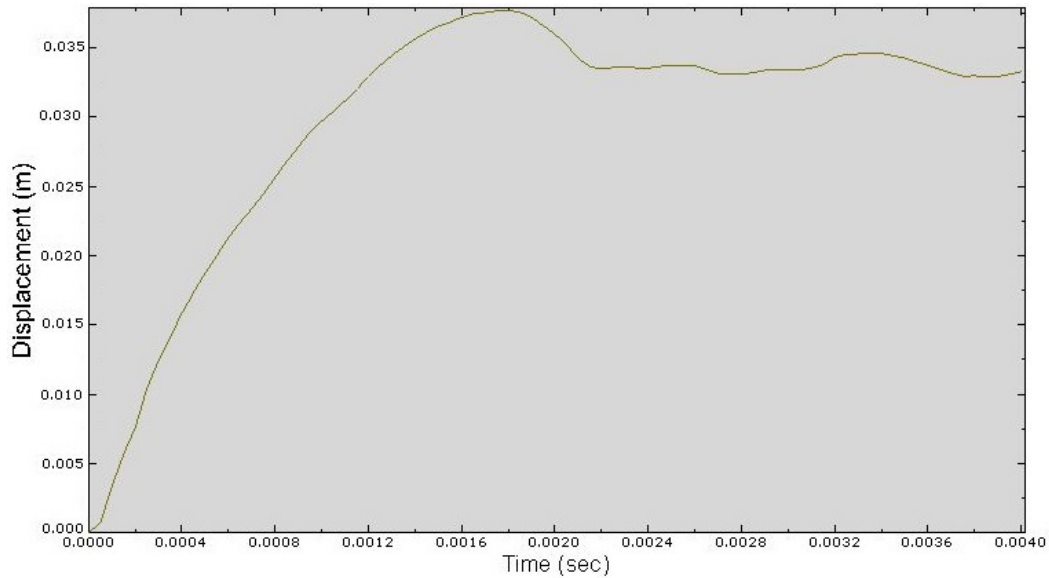
Figure 19: Displacement vs. Time, CEL Bird Impactor, at V = 150 m/s

B. Sandwhich Panel Material Model Validation

Experimental data of low velocity and ballistic impacts are widely available in the literature. On the other hand, the experimental data for the bird strike is limited and only a small number of references provide experimental results of such impacts on composite plates. For the current analysis where the bird strike on sandwich composite panel was the prime interest, the validation of the material model was done by projecting a rigid steel sphere over a square composite sandwich panel (140 mm x 140 mm x 24 mm) [40]. The skins were 2 mm thick, and of woven laminate of carbon fibers AS4 and epoxy 8552. The core was a 3003 aluminum honeycomb of 20 mm thick and 77 kg/m^3 in density. Figure 20 shows the finite element discretization of the composite panel. The skins were modeled using 1225 conventional shell elements (S4R), and 3136 solid elements (C3D8R) were used for the core. The steel sphere was modeled as a rigid body.
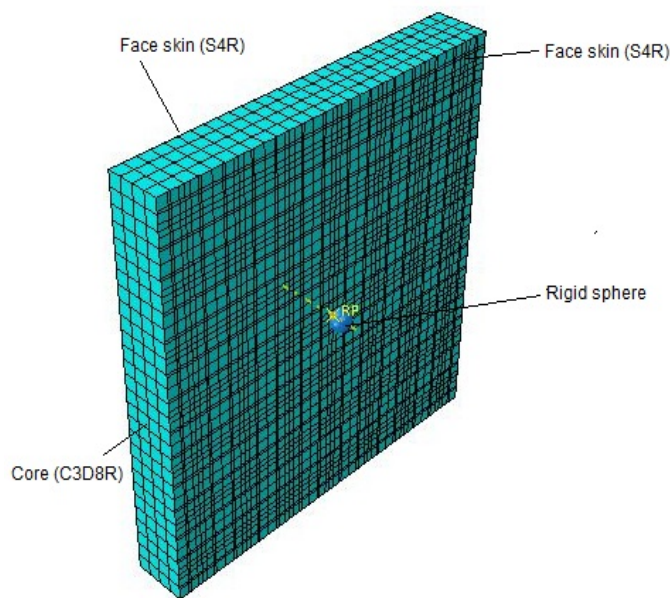
Figure 20: Sandwich panel verification setup

27

The specimen was impacted by spherical steel projectile of 1.7 g and 7.5 mm in diameter. Four impact speeds, 200, 250, 300, and 400 m/s, were used for numerical analysis. The variable selected to validate the finite element model was a residual velocity (velocity after impact) of the rigid steel sphere. Figure 21 shows experimental and numerical residual velocities as a function of the impact velocities. Numerical results were close to the experimental data. Hence, the material failure and damage models used for the CFRP skins and honeycomb core are verified.
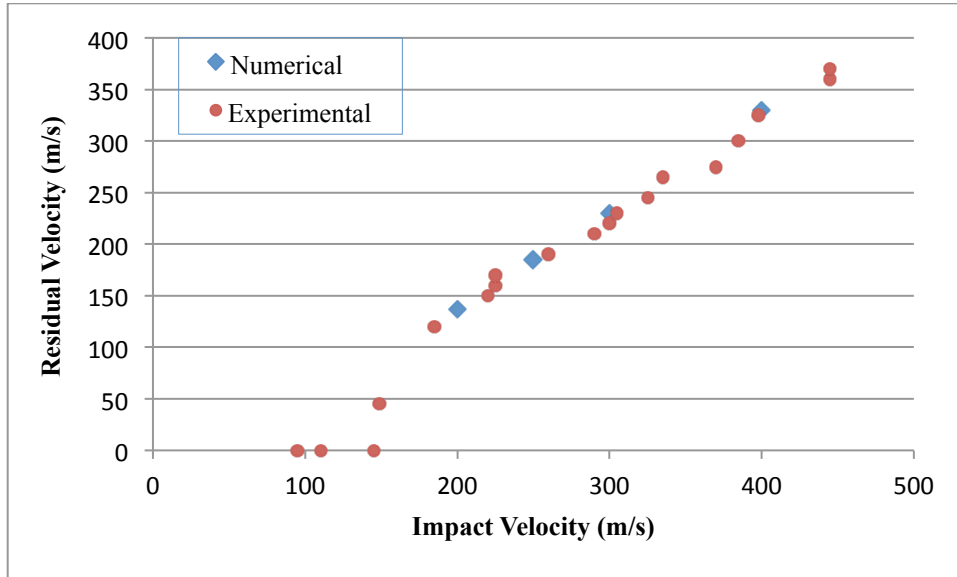

Figure 21: Residual velocity versus Impact velocity

IX.   CEL Bird Impact Analysis

After validations of the bird model and sandwich honeycomb panel model, the bird impact analysis on the leading edge was performed using Coupled Eulerian Lagrangian approach. Figure 22 shows the model setup in Abaqus/Explicit environment. It is appeared that only some portion of the wing leading edge is enclosed by a eulerian domain. This is because the purpose of the eulerian domain is to predict the motion of the bird material. Hence, dimensions of the eulerian domain were chosen in such a way that it captured the bird motion throughout its motion. This also reduces computational time, as there are less eulerian elements. There are total 180565 eulerian elements in the model.
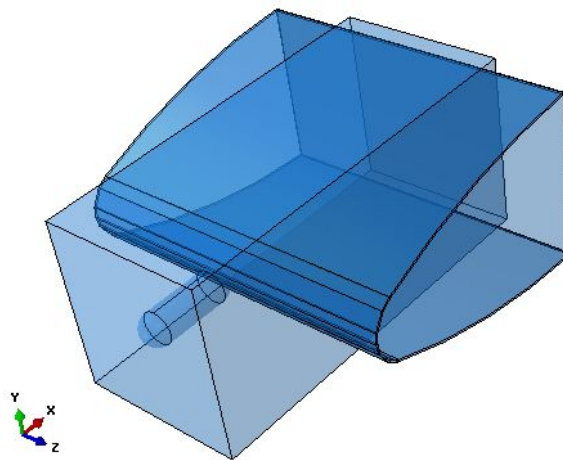

Figure 22: CEL model of leading edge bird strike analysis

28

As described earlier, the FAR 25.571 regulation requires an aircraft wing leading edge to withstand an impact of a 4 lb (1.81 kg) bird at 287 knots (148 m/s). The kinetic energy of a 4 lb bird at an impacting speed of 148 m/s is sufficient to cause severe damage on the leading edge. In this paper, to demonstrate the difference in energy absorbing capability of two honeycomb cores, the bird impact analysis on two wing leading edge configurations was done.

A.   Results (ACG-1/4 core and CFRP skins)

Figure 23 shows the bird strike event on the wing leading edge with CFRP skins and ACG-1/4 core at different time interval. The stresses generated due to impact are higher than the material strength of the composite skins and core. Therefore, the bird penetrates through the wing leading edge and strikes against the front spar. However, all the members of the wing leading edge, such as core, and top and bottom skins, have absorbed some of the kinetic energy of the bird. That reduces its velocity, and in consequence, the stresses generated due to further impact of the bird with the front spar are lower than the spar material strength. Hence, the main load caring member of the wing has survived the impact, and remained critically unharmed from the bird strike.

t = 0 sec

t = 0.0015 sec

t = 0.0045 sec

t = 0.00581 sec

t = 0.00656 sec

t = 0.0075 sec
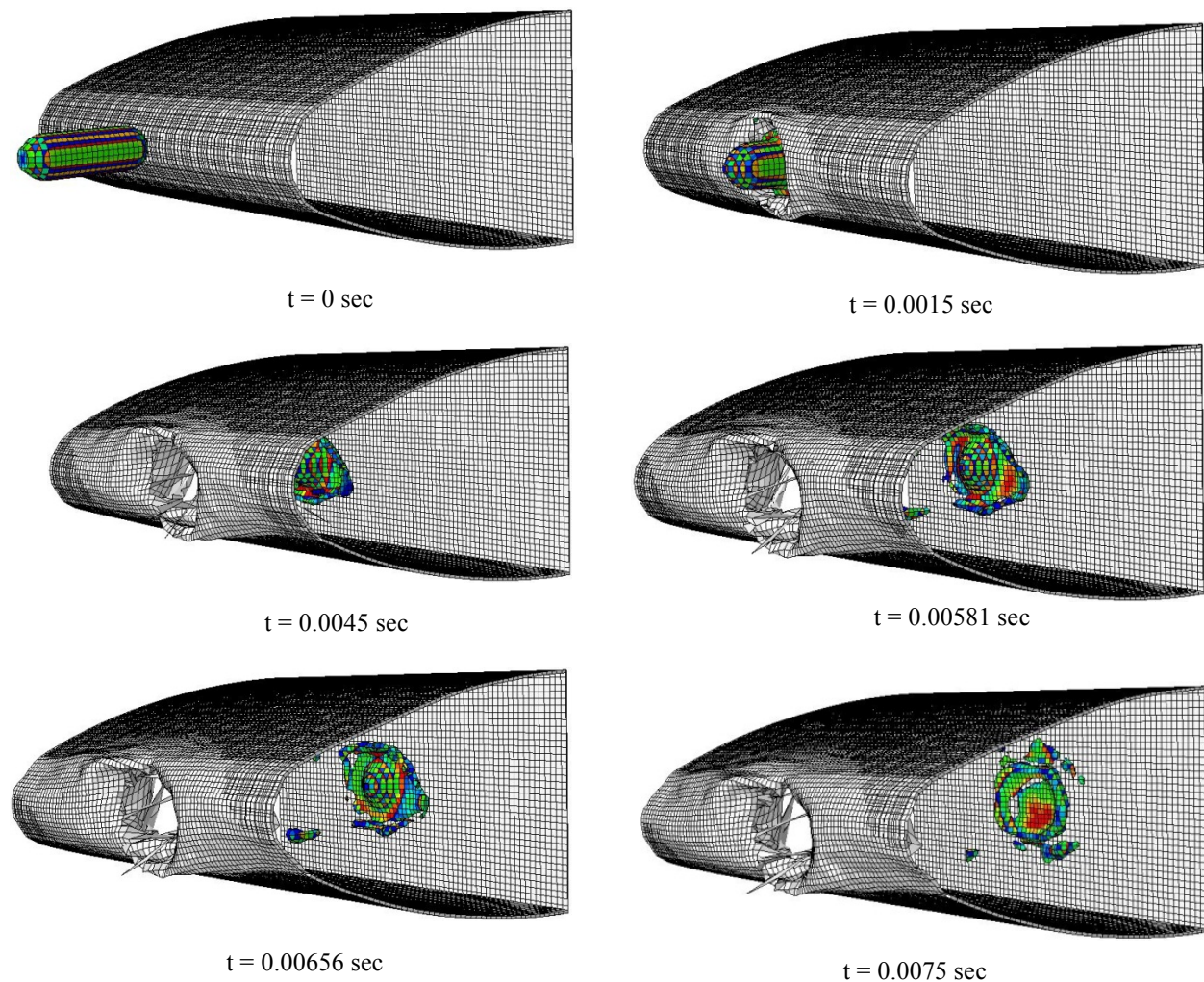
Figure 23: Bird strike event at different time interval (ACG-1/4 core and CFRP skin)

As discussed earlier, the Hashin failure criterion identifies four different failure modes of composite ply. As illustrated, the bird penetrates the wing leading edge and impacts on the front spar. This results into the onset of tensile and compressive stresses in the top and bottom composite skins of the sandwich structure. Figure 24 shows

composite material failure modes, such as fiber tensile and compressive, and matrix tensile and compressive. It is appeared that the dominant failure mode of the composite skin is tensile matrix failure.
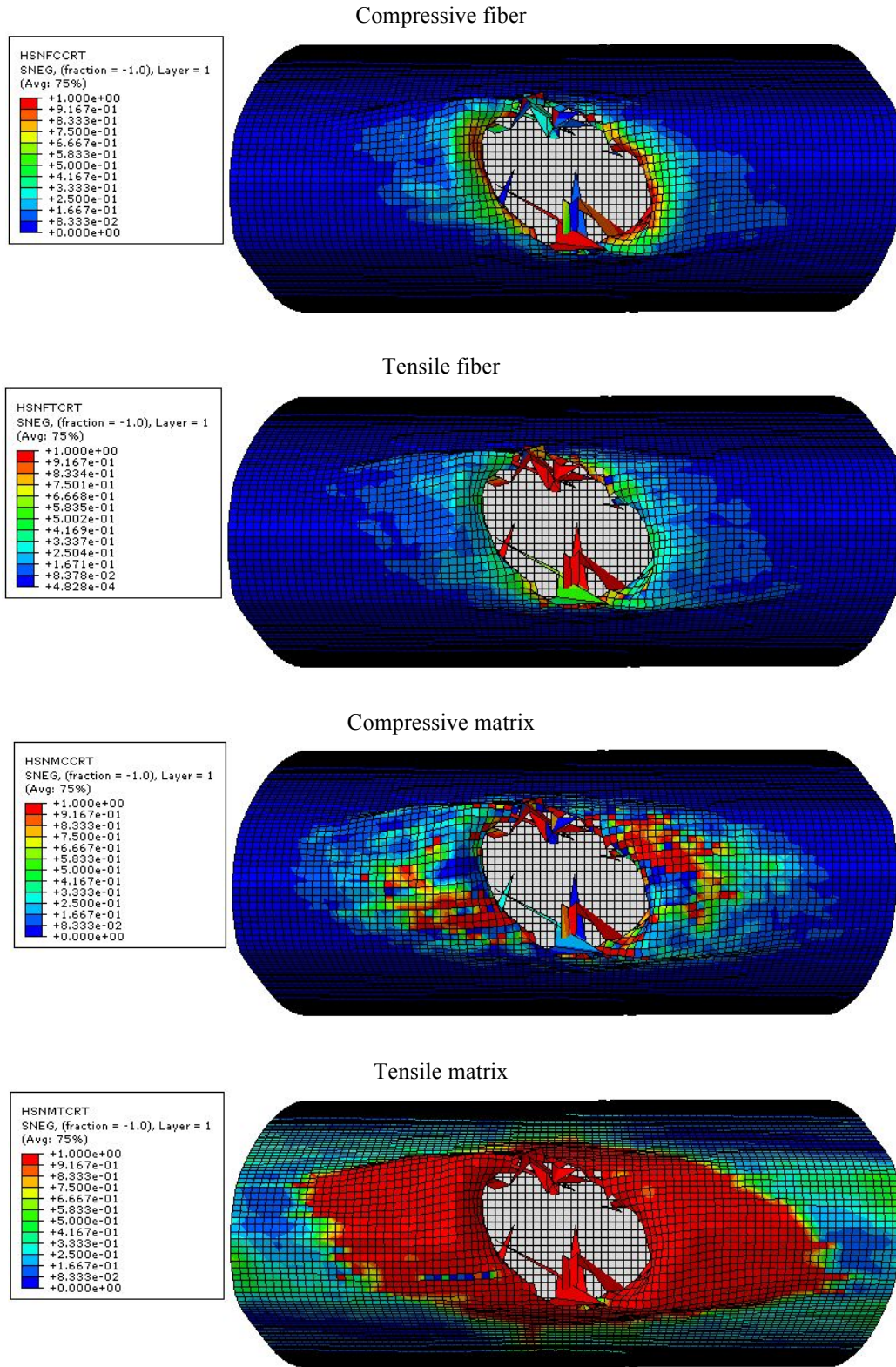
Compressive fiber

Tensile fiber

Compressive matrix

Tensile matrix

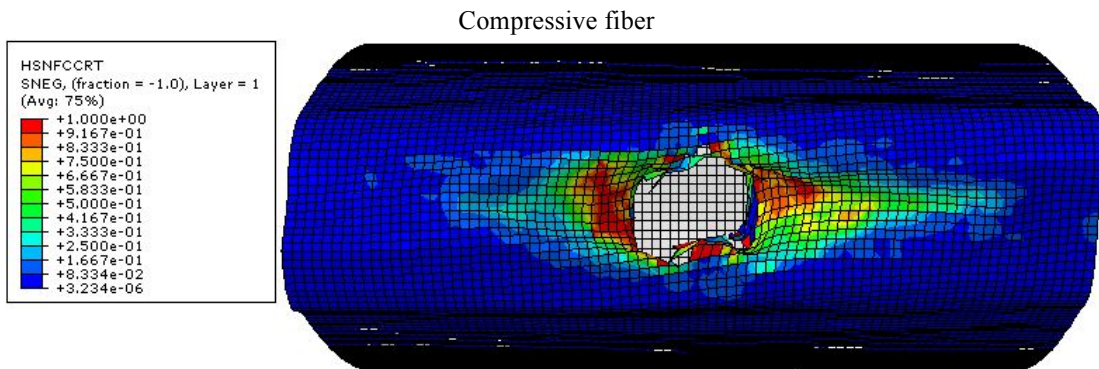**Figure 24: Composite top skin failure modes (ACG-1/4 core and CFRP skins)**

B. Results (ACG-1 core and CFRP skins)

In the second impact scenario, the bird impact analysis was performed on the ACG-1 core and CFRP skins sandwich wing leading edge. Like previous case, the bird penetrates through the leading edge and strikes against the front spar. The impact event at different time interval is shown in Figure 25.

t = 0 sec

t = 0.00154 sec

t = 0.00327 sec

t = 0.00404 sec

t = 0.00616 sec

t = 0.0077 sec
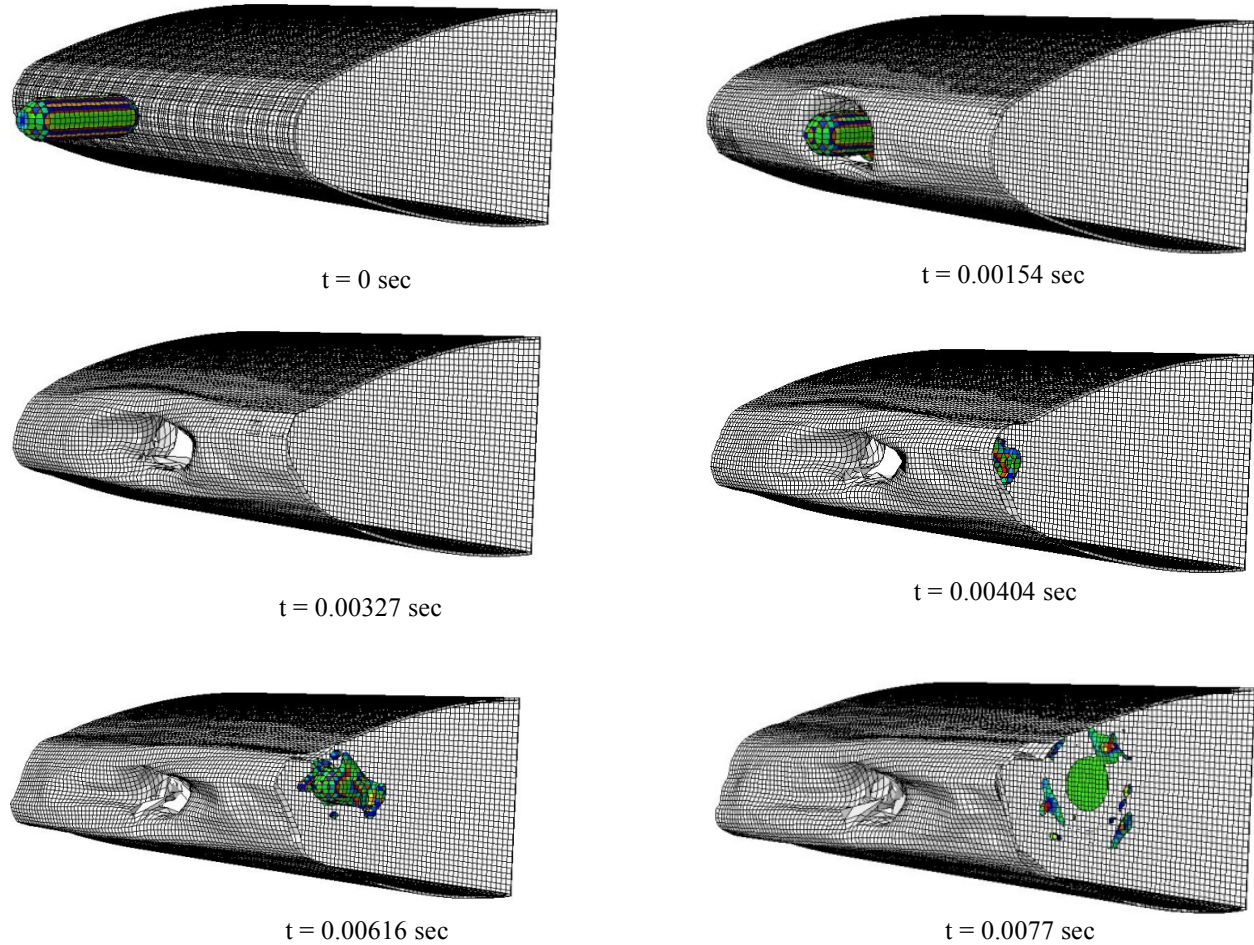
Figure 25: Bird strike event at different time interval (ACG-1 core and CFRP skins)

Figure 26 shows composite material failure modes. In this case, the dominant composite failure mode is also matrix tensile failure mode.
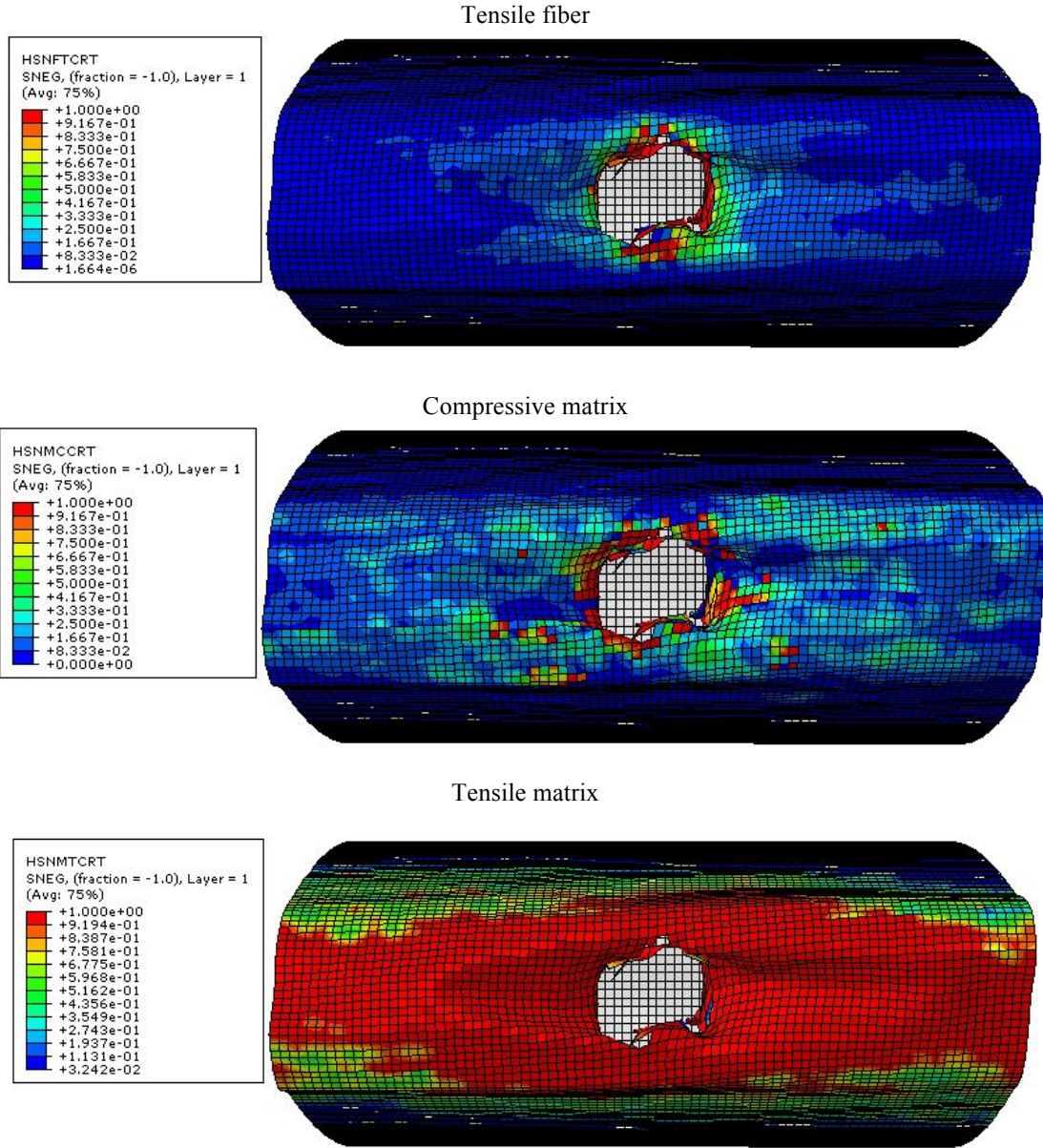
Compressive fiber

Tensile fiber

Compressive matrix

Tensile matrix

Figure 26: Composite top skin failure modes (ACG-1 core and CFRP skins)

C. Energy balance

To ensure that there were no numerical errors within the developed models, the energy equation was checked to ensure that it was in a balanced state. The following energy equation must hold true at all times during an analysis and is given by

$$E_{total} = E_I + E_V + E_{KE} + E_{FD} - E_W \tag{42}$$

In the present analyses, it is assumed that the bird is made out of incompressible water and the frictional losses between the bird and structure is negligible. Therefore, viscous energy dissipation (E_V), and frictional energy dissipation (E_{FD}) become zero in Equation (42). The internal energy, given by Equation (43), is the sum of the recoverable elastic strain energy (E_E), the energy dissipation through plasticity (E_P), the energy dissipation through viscoelasticity or creep (E_{CD}), and the artificial strain energy (E_A).

$$E_I = E_E + E_P + E_{CD} + E_A \tag{43}$$

The artificial strain energy is the energy associated with solid and shell elements undergoing hourglass modes of deformation. Since hourglassing is a purely numerical occurrence having no corresponding physical phenomenon. It is important that the size of the hourglass energy term remain very small relative to the overall system energy throughout a simulation. If hourglass energy becomes a significant portion of the overall system energy balance, this is an indication that non-physical phenomena are unduly influencing the simulation. In such situations, the results should be regarded as potentially unreliable.

Figure 27 and 28 show the energy balance charts for the wing leading edge with ACG-1/4 core and ACG-1 core respectively. In both cases, the artificial strain energy is comparatively low in value throughout the impact event. Therefore, no energy is introduced or absorbed artificially that may be generated due to numerical instability, and each model is in a balanced state.
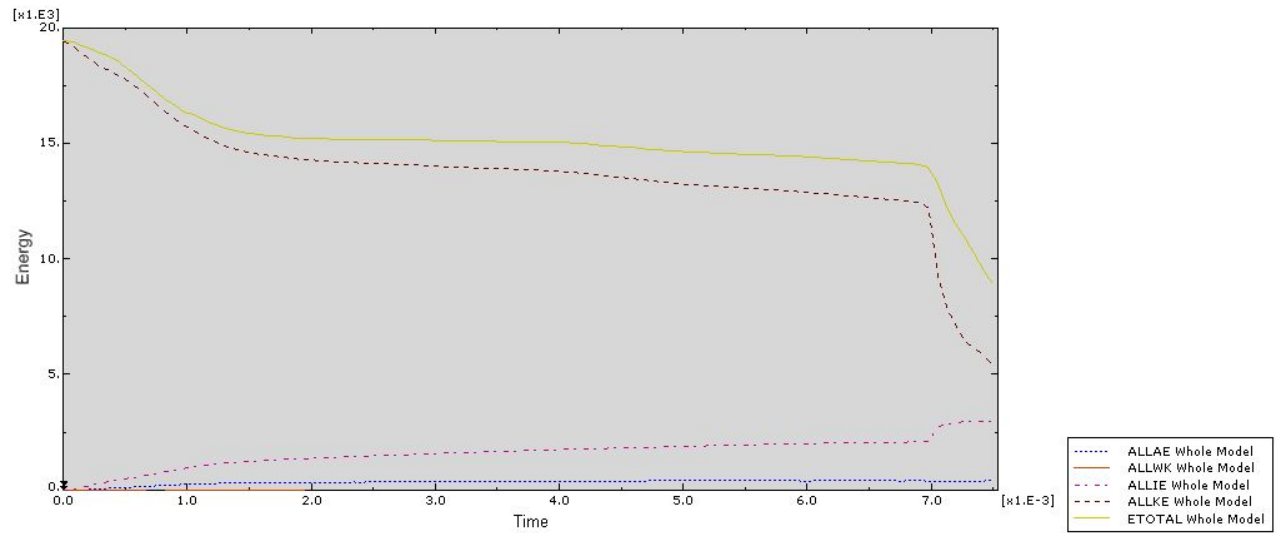

Figure 27: Energy balance chart for the wing leading edge (CFRP skins and ACG-1/4 core)
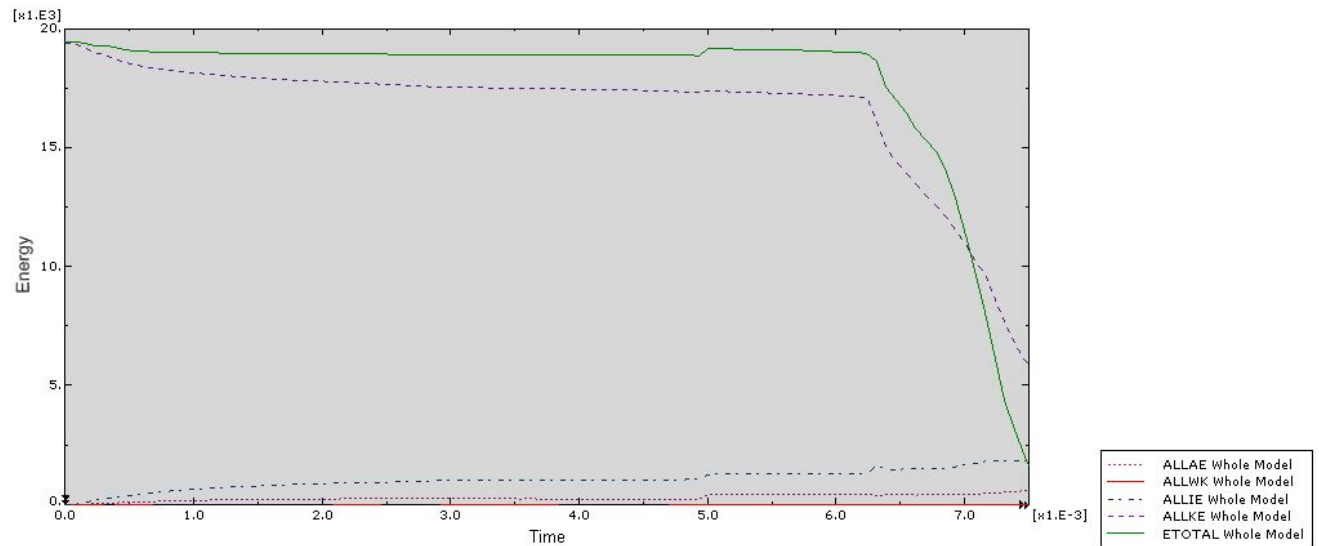

Figure 28: Energy balance chart for the wing leading edge (CFRP skins and ACG-1 core)

D. Core comparison

In both cases, the front spar deforms due to its collision with the bird. The amount of deformation depends on the remaining kinetic energy of the bird after penetrating through the wing leading edge. Figure 29 and 30 show the deflection contours for the wing leading edge with ACG-1/4 core and ACG-1 core respectively. The maximum deflection is at the center point of impact shown by red area in the following figures. For the ACG-1/4 core, the maximum deflection is 0.577 mm, and for ACG-1, it is 2.05 mm. The difference in deflections is because of the difference in energy absorbing capabilities of each core. ACG-1/4 being highly dense and strong absorbs more kinetic energy than ACG-1 core. As the density of the core increases, its energy absorbing capacity also increases. Vice-a-versa, as it decreases, its capability of absorbing kinetic energy reduces too.
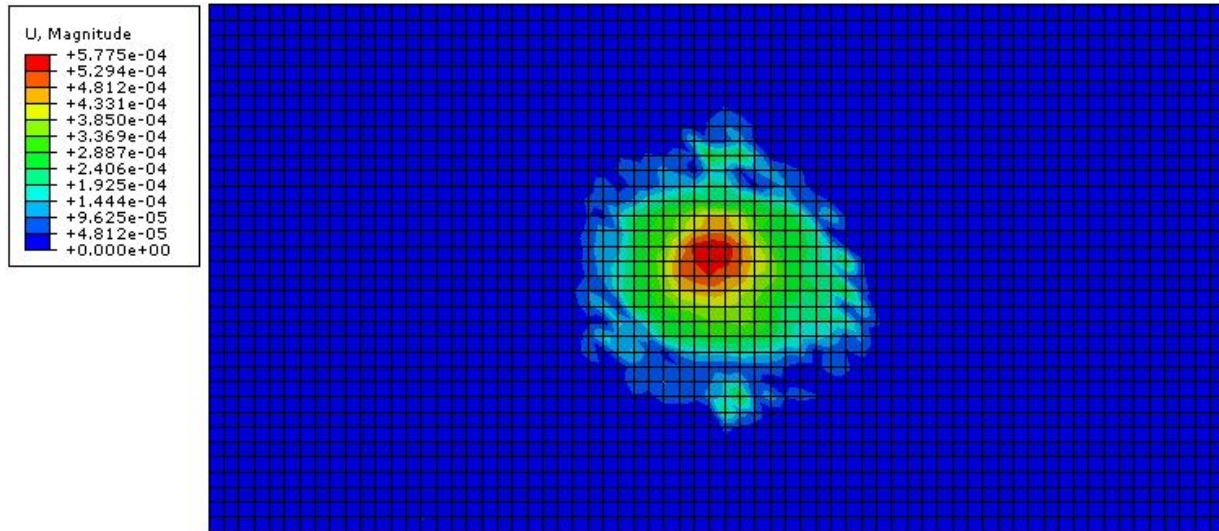

Figure 29: Front spar deflection due to bird impact (ACG-1/4 core and CFRP skins)
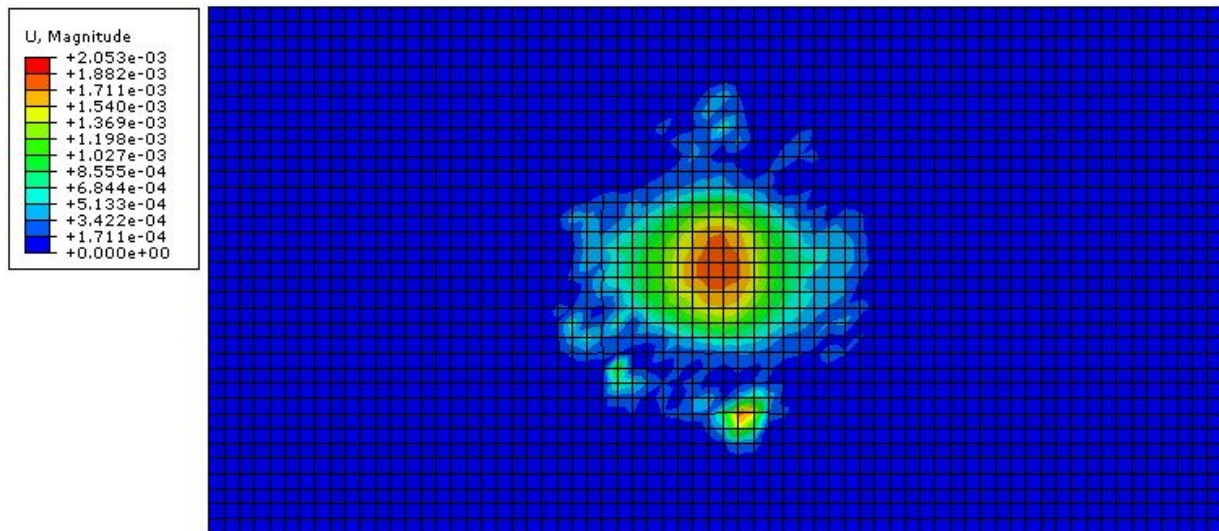

Figure 30: Front spar deflection due to bird impact (ACG-1 core and CFRP skins)

The stress vs. strain curve for ACG-1/4 honeycomb core is shown in Figure 31. The crushing of the core takes place once the stresses exceed material yield strength of the core. Then, the progressive crushing of core begins until the core fails at about 81.3% strain. Similarly, for ACG-1 honeycomb core, the stress vs. strain curve is given in Figure 32. ACG-1 core fails when the strain is about 70%.
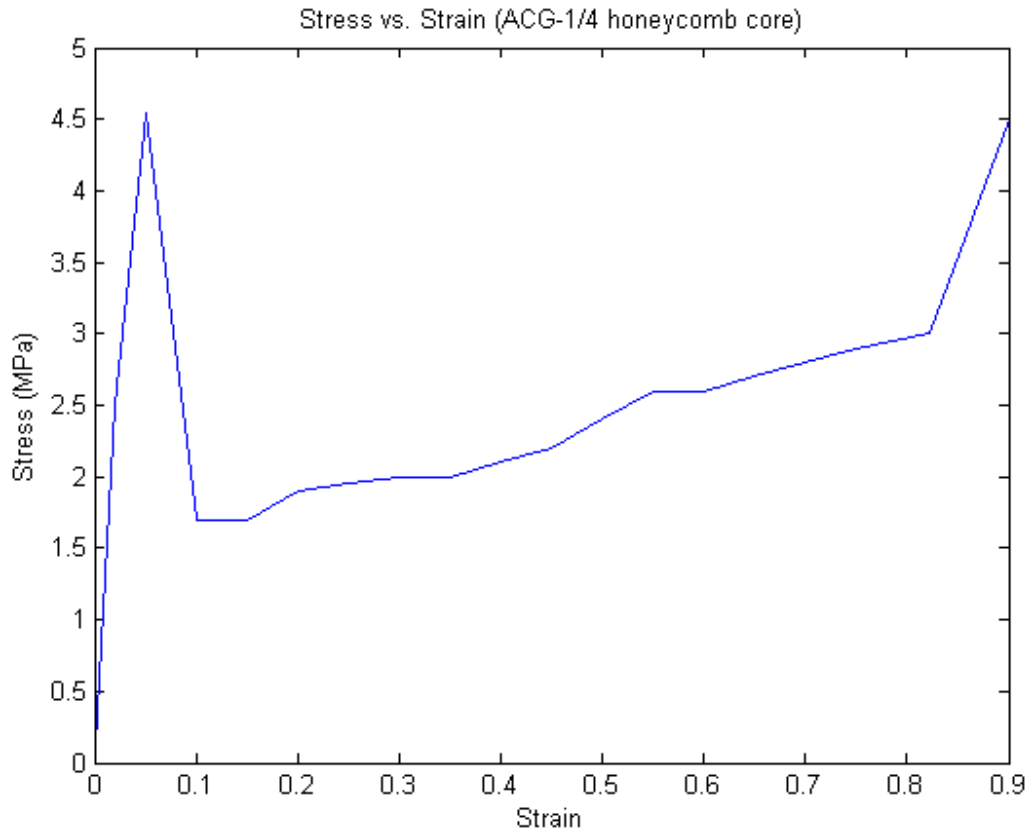
Figure 31: Stress vs. Strain curve for ACG-1/4 honeycomb core
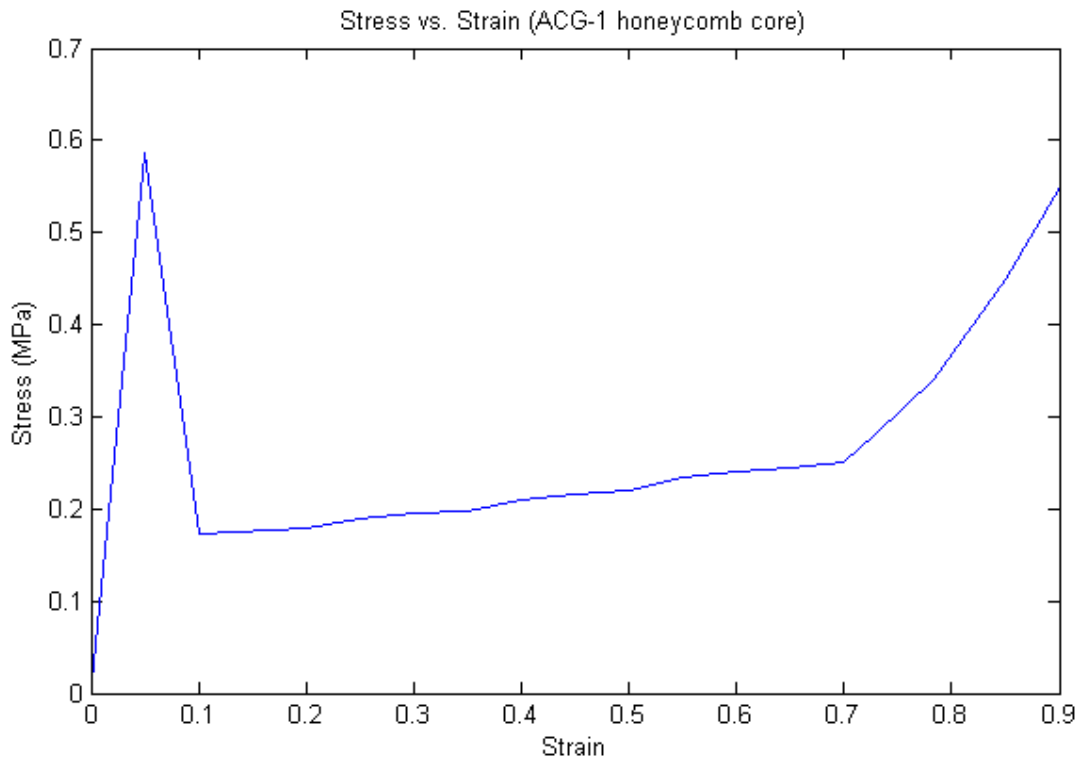

Figure 32: Stress vs. Strain curve for ACG-1 honeycomb core

Figure 33 and 34 show kinetic energy absorbed by each member of the sandwich panel. The core absorbed more kinetic energy than top and bottom skins. For the sandwich panel with ACG-1/4 core, the kinetic energy dissipated into core material is approximately 90% of the total energy absorbed by the wing leading edge, while fore the sandwich panel with ACG-1 core, it is 80% of the total energy.
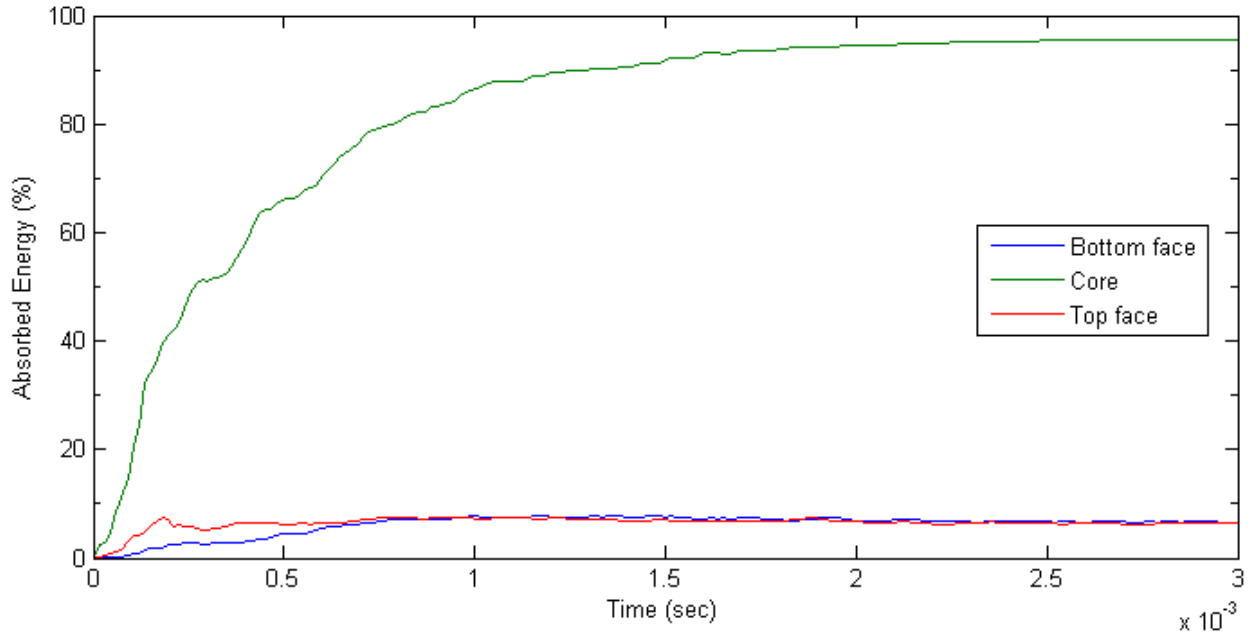
Figure 33: Kinetic energy absorbed vs. Time (ACG-1/4 core and CFRP skins)
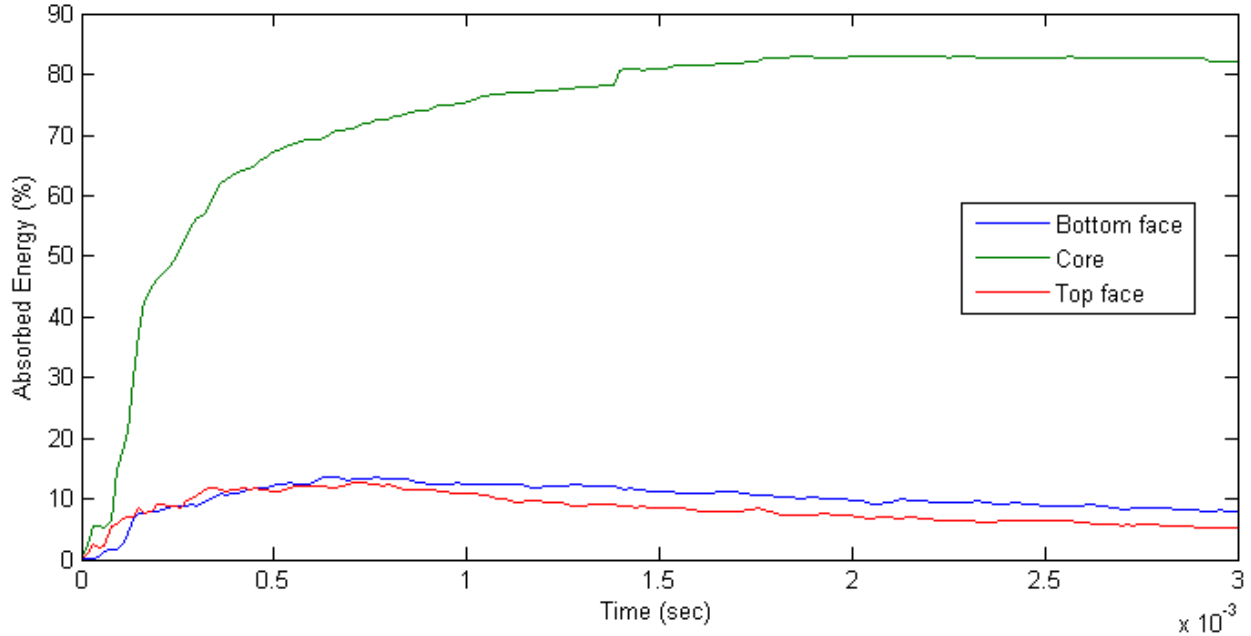
Figure 34: Kinetic energy absorbed vs. Time (ACG-1 core and CFRP skins)

X.   Conclusion

A numerical analysis procedure for simulating the soft body impact response of sandwich honeycomb wing leading edge using finite element codes has been presented. The present formulation has been used to predict the transient response of laminated composite skins and honeycomb core. It has been proved that the hemi-spherical bird shape resembles the response of actual birds during experimental tests. Validation cases for the bird and

sandwich panel models show that the results of the analyses are very close to experimental results. It is also verified that the coupled eulerian lagrangian approach is more accurate than the lagrangian approach when there is a solid-fluid interaction in an analysis. In this paper, two sandwich panels with different cores have been analyzed to compare their impact behavior. In both cases, the dominant failure mode of the composite skin is matrix tensile failure. In addition, analyses show that the core energy absorbing capability depends on cell size, core type, and thickness. Hence, in the present work, highly dense ACG-1/4 core absorbed more kinetic energy than ACG-1 core.

XI.   Bibliography

[1]   Wilbeck, J.S. Impact Behavior of Low Strength Projectiles. Air Force Materials Laboratory, Technical Report AFML-TR-77-134, 1977.

[2]   Welsh C.J. and Centoze V., "Aircraft Transparency Testing – Artificial Birds" Arnold Engineering Development Center, Report AEDC-TR-86-2, 1986

[3]   Smojver I, Ivancevic D., Mihaljevic D., "An Explicit Numerical Modeling of Soft Body Impact Damage in Metallic Airplane Structures" , CMES, Vol. 70, No. 2, pp. 191-215, 2010

[4]   Smojver I, Ivancevic D., "Coupled Euler Lagrangian Approach Using Abaqus/Explicit in the Bird Strike Aircraft Damage Analysis", 2010 Simulia Customer Conference

[5]   Smojver I, Ivancevic D., "High Velocity Impact Damage in Composite Aeronautical Structures-Numerical Model"

[6]   Design Airspeeds," Part 25 Airworthiness Standards: Transport Category Airplanes, Federal Aviation Administration, Dept. of Transportation, Sec. 25.571, Washington, D.C., 2003

[7]   Heimbs, S., "Bird Strike Analysis in Aircraft Engineering: An Overview ", In: Advances in Mechanical Engineering Research, Volume 3, D.E. Malach (ed.), Nova Science Publishers, New York, 2011

[8]   John L. K., "Wing Leading Edge Design with Composites to Meet Bird Strike Requirements", in: Strong, A. B. (Ed.), Composites in Manufacturing – Case Studies, SME, Dearborn, 1991, pp. 3-18

[9]   Airoldi A., and B. Cacchione, "Modeling of Impact Forces and Pressures in Lagrangian Bird Strike Analyses", International Journal of Impact Engineering, no. 32, pp. 1651-1677, 2006

[10]   McCarthy M.A, Xiao J.R., Petrinic N, Kamoulakos A. and Melito. A " Modeling of bird Strike on an Aircraft Wing Leading Edge Made from Fiber Metal Laminates - Part 1: Material Modeling", Applied Composite Materials 11: 295-315, 2004

[11]   Erkan Kirtil, Dieter Pestal, Alexander Kollofrath, Nils Gansicke, Josef Mendler, "Simulating the Impact Behavior of Composite Aircraft Structures", 2003 Abaqus Users Conference

[12]   Villanueva G. R., Cantwell W. J., "The high velocity impact response of composite and FML – reinforced sandwich structures", The University of Liverpool, Liverpool, UK, 2003

[13]   Vaidya UK, Nelson S., Sinn B., Mathew B., ''Processing and high strain rate impact response of multi-funtional sandwich composites'', Compos Struct 2001;52:429-40

[14]   Harte AM, Fleck NA, Ashby MF, "Sandwich panel design using aluminum alloy foam", Advanced Engineering Materials 2000; 2(4):219-22

[15]   McCormack TM, Miller R, Kesler O, Gibson LG, "Failure of sandwich beams with metallic foam cores", International Journal of Solids and Structures 2001;38:4901-20

[16]   Kunimoto T, Mori N. Study on the buffer characteristics of the corrugated-core used for the 5051 aluminum alloy sandwich construction under dynamic loading. J Light Met 1989; 39 (10): 687–92

[17]   Chizari, M., L.M. Barrett and S.T.S Al-Hassani, "An Explicit Numerical Modelling of the Water Jet Tube Formin'', Computational Materials Science, no. 45, pp. 378-384, 2009

[18]   John O'Callaghan, "Bird-Strike Certification Standards and Damage Mitigation", National Transportation Safetry Board (NTSB) report

[19]   Georgiadis S, Gunnion AJ, Thomson RS, Cartwright BK, ''Bird-strike simulation for certification of the Boeing 787 composite moveable trailing edge'', Compos Struct 2008;86:258–68

[20]   Understanding and reducing bird and other wildlife hazards to Aircrafts, Bird Strike Committee USA, 2009

[21]   Aktay L, Johnson AF, Holzapfel M., ''Prediction of impact damage on sandwich composite panels'', Comput Mater Sci 2005; 32: 252-60

[22]   National Aerospace Laboratory, Technical report, ''Design and Testing of a Composite Birdstrike resistant leading edge'', SAMPE Europe Conference & Exhibition, Paris, France, April 2003

[23] ''LS Dyna User manual V971'', Livermore Software Technology Corporation, 2009

[24] Peterson R. L., and Barber J. P., ''Bird Impact Forces in Aircraft Windshield Design'', Report # AFFDL – TR-75-150, March, 1976

[25] A publication of shock and vibration information center, U.S. Naval Research Laboratory, Washington D.C: The shock and Vibration bulletin, 1978

[26] Baughn T. N., and Graham L. W., ''Simulation of Birdstrike Impact on Aircraft Canopy Material'', Journal of Aircraft, Vol. 25, No. 7, pp 659-664, July 1988

[27] Hallquist J. O., Theoretical Manual, Livermore Software Technology Corporation, March, 2006

[28] Belytschko T., Liu W. K., and Moran B., ''Nonlinear Finite Elements for Continua and Structure'', John Wiley & Sons Ltd., 2000

[29] Brockman R. A., and Held T. W., ''Explicit Finite Element Method for Transparency Impact Analysis'', University of Dayton Research Institute, Dayton, Ohio, June 1991

[30] Johnson AF, Holzapfel M., ''Modeling soft body impact on composite structures'', Compos Struct 2003;63:103-13

[31] Research Paper, ''The Hazard Posed to Aircraft by Birds'', Australian Transport Safety Bureau, 2002

[32] Metallic materials and elements for aerospace vehicle strcutures, MIL-HDBK-5, Department of Defence Handbook, Washington D.C: 2003

[33] Abaqus analysis user's manual, Version 6.11. Dassault Systemes; 2011

[34] Abrate S. Impact on composite structures. Cambridge: Cambridge University Press; 1998. P.242-57

[35] Hexcel Corporation, "Honeycomb Sandwich Design Technology", Dublin, CA, USA

[36] Hexcel Corporation, "Honeycomb Attributes and Properties", Dublin, CA, USA

[37] Wahl, L.; Maas, S.; Waldmann, D.; Zurbes, A.; Freres, P., "Shear stresses in honeycomb sandwich plates: Analytical solution, finite element method and experimental verification", Journal of Sandwich Structures and Materials 14 (4): 449-468

[38] V. Mollon, J. Bonhomme, J. Vina, A. Arguelles, A. Fernandez-Canteli, "Influence of the principal tensile stresses on delamination fracture mechanisms and their associated morphology for different loading modes in carbon/epoxy composites"

[39] M. Meo, R. Vignjevic, G. Marengo, "The response of honeycomb sandwich panels under low-velocity impact loading"

[40] Brenda L. Buitrago, Carlos Santiuste, Sonia Sanchez-Saez, Enrique Barbero, Carlos Navarro, "Modeling of composite sandwich structures with honeycomb core subjected to high velocity impact"

[41] FAA Special Project Number SP4614WI-Q, "Hexcel 8552 AS4 Unidirectional Prepreg at 190 gsm & 35% RC Qualification Material Property Data Report", NCAMP Test Report Number CAM-RP-2010-002, Rev A

[42] National Aeronautics and Space Administration, "A study of failure criteria of fibrous composite materials", NASA/CR-2001-210661, March 2001